INT. J. NUM. METH. HEAT FLUID FLOW, VOL. 3, 483–516 (1993)

TVD FINITE-DIFFERENCE METHODS FOR COMPUTING HIGH-SPEED THERMAL AND CHEMICAL NON-EQUILIBRIUM FLOWS WITH STRONG SHOCKS

C. P. T. GROTH* AND J. J. GOTTLIEB

Institute for Aerospace Studies, University of Toronto, 4925 Dufferin Street, Downsview, Ontario, Canada M3H 5T6

ABSTRACT

Partially-decoupled upwind-based total-variation-diminishing (TVD) finite-difference schemes for the solution of the conservation laws governing two-dimensional non-equilibrium vibrationally relaxing and chemically reacting flows of thermally-perfect gaseous mixtures are presented. In these methods, a novel partially-decoupled flux-difference splitting approach is adopted. The fluid conservation laws and species concentration and vibrational energy equations are decoupled by means of a frozen flow approximation. The resulting partially-decoupled gas-dynamic and thermodynamic subsystems are then solved alternately in a lagged manner within a time marching procedure, thereby providing explicit coupling between the two equation sets. Both time-split semi-implicit and factored implicit flux-limited TVD upwind schemes are described. The semi-implicit formulation is more appropriate for unsteady applications whereas the factored implicit form is useful for obtaining steady-state solutions. Extensions of Roe's approximate Riemann solvers, giving the eigenvalues and eigenvectors of the fully coupled systems, are used to evaluate the numerical flux functions. Additional modifications to the Riemann solutions are also described which ensure that the approximate solutions are not aphysical. The proposed partially-decoupled methods are shown to have several computational advantages over chemistry-split and fully coupled techniques. Furthermore, numerical results for single, complex, and double Mach reflection flows, as well as corner-expansion and blunt-body flows, using a five-species four-temperature model for air demonstrate the capabilities of the methods.

KEY WORDS TVD schemes Thermochemical non-equilibrium flows Approximate Riemann solvers Flux difference splitting

INTRODUCTION

The physics of hypersonic flow is significantly different from that of the subsonic, transonic, and supersonic flow regimes. Strong shocks and very high temperatures are two distinctive characteristics of the hypersonic flow environment. The high temperatures result in non-ideal thermodynamic behaviour of air and other gases. For relatively high-density hypersonic flows (normally encountered in atmospheric flight at lower altitudes), molecular and atomic mean free paths are such that collisional rates are high. In these cases, the Damköhler number *Da*, defined to be the ratio of the convection or advection time scale to the time scales associated with the thermal and chemical processes, approaches infinity and a gas may be modelled as if it were in thermodynamic equilibrium. However, for lower density hypersonic flows (usually encountered in atmospheric flight at higher altitudes) in which the continuum assumption still

* Current address: Department of Aerospace Engineering, University of Michigan, Ann Arbor, Michigan 48109, USA.

0961–5539/93/060483–34$2.00

Received April 1992
Revised March 1993

applies but molecular collisional rates are sufficiently low, the Damköhler number is finite and the fluid cannot always maintain thermodynamic equilibrium. In these cases, non-equilibrium effects, such as finite-rate vibrational and chemical processes, become important and must be considered. With the present renewed interest in hypersonic aerodynamics, efficient and accurate numerical methods are required for the prediction of high-speed flows characterized by strong shocks and finite-rate thermodynamic processes.

In general, the computation of weak solutions to flow problems with strong discontinuities necessitates special consideration. Classical first-order shock-capturing schemes require excessive grid refinement to resolve the complicated shock structure and second-order schemes lead to spurious Gibb's-like oscillations or non-linear instabilities near the discontinuities. For these reasons improved solution techniques were sought and, in the last 10–15 years, innovative advances in shock-capturing techniques for hyperbolic conservation laws have led to the development of several high-resolution numerical schemes for the solution of multidimensional flows of polytropic gases (thermally and calorically perfect). Examples of the more powerful and popular techniques are the flux-corrected transport (FCT) method of Boris and Book[1], monotonic upstream-centred scheme for conservation laws (MUSCL) of van Leer[2], piecewise parabolic method (PPM) of Colella and Woodward[3], generalized Riemann problem (GRP) method of Ben-Artzi and Falcovitz[4], upwind and symmetric total-variation-diminishing (TVD) schemes of Harten[5,6], Roe[7–9], Davis[10], Yee[11,12], and Osher and Chakravarthy[13–15], and the essentially non-oscillatory (ENO) schemes of Harten, Enquist, Osher, and Chakravarthy[16]. These solution-dependent (i.e., non-linear) explicit and implicit time-stepping methods provide monotonic oscillation-free solutions and increased accuracy near discontinuities, such as shock waves, contact surfaces, and slip streams. They are, therefore, appropriate for steady and unsteady hypersonic flow applications; however, extended versions of the algorithms are necessary for the study of flows with high-temperature and real-gas phenomena.

A number of the aforementioned modern shock-capturing schemes have been extended to include equilibrium high-temperature and real-gas effects[17–25]. Provided that the thermodynamic properties are evaluated in an efficient manner, these equilibrium solvers are computationally efficient and provide sharp resolution of discontinuities.

Extensions of the shock-capturing techniques for non-equilibrium flows require more attention. To account for the various species and internal energy modes of gaseous flows predominated by finite-rate thermodynamic processes, numerical solutions satisfying monotonicity, positivity, and maximum principles are required for large systems of conservation laws with often large source terms. In many cases, the large source terms make the solution algorithms stiff (i.e., as in the solution of stiff systems of ordinary differential equations, the time-stepping of a marching procedure is drastically constrained by stability considerations rather than by the usual accuracy concerns). This is problematic because the computational requirements for solving large systems with inherent numerical stiffness may become enormous. Furthermore, LeVeque and Yee[26], as well as Griffiths, Stuart, and Yee[27], indicate that if the source terms are sufficiently stiff then numerical schemes may propagate solution discontinuities, such as shocks, at incorrect or aphysical wave speeds. Thus, shock-capturing schemes for non-equilibrium flows must be designed to provide accurate results in an efficient manner.

Several explicit, semi-implicit, and fully implicit time-stepping MUSCL-type and TVD approaches have been devised for the prediction of non-equilibrium flows. Eberhardt and Brown[28] extended a first-order explicit TVD upwind scheme for investigating chemically reacting flows. A fourth-order Runge–Kutta time-differencing of the source terms was employed to enhance the numerical stability and the gas-dynamic and species conservation equations were solved in a fully coupled (simultaneous) manner. Glaz *et al.*[29] have developed an explicit second-order Godunov (MUSCL-like) method for predicting non-equilibrium vibrationally relaxing and chemically reacting flows of air, in which the gas-dynamic and thermodynamic equations are solved in a time-split (decoupled) fashion. Ben-Artzi[30] also describes a reformulation of the explicit GRP method for chemically reacting flows. Again, explicit

differencing procedures (second- and fourth-order Runge–Kutta) for the source terms were used in both of these methods. In other studies, Liu and Vinokur[31] and Shuen *et al.*[32] considered the most general case of non-equilibrium flow and present formulae for the numerical evaluation of the inviscid fluxes using several popular upwind flux-splitting methods.

The explicit time-stepping schemes described above are valid for either time-accurate or steady-state calculations of non-equilibrium flows. However, the stiffness of the source terms may force the time step sizes of the explicit schemes to be excessively small and the corresponding computer times to be prohibitively large, especially for steady-state computations. Thus, implicit solvers for non-equilibrium flows have also been formulated. In these methods, the numerical stability is enhanced by treating some or all terms implicitly. Yee and Shinn[33] and Ben-Artzi[30] propose fully coupled semi-implicit extensions of symmetric TVD and GRP techniques, respectively, for the computation of chemically reacting flows. These schemes treat only the source terms implicitly and, therefore, avoid large matrix inversions. They are similar to the semi-implicit methods described by Bussing and Murman[34].

Gnoffo and McCandless[35], Gnoffo, McCandless, and Yee[36], and Gnoffo[37] have proposed both loosely and fully coupled fully implicit algorithms which use a second-order symmetric TVD scheme of Yee[11,12] to solve steady viscous hypersonic flows of air and include the effects of vibrational relaxation, dissociation/recombination, and ionization. Similar fully implicit procedures are discussed by Yee and Shinn[33] for chemically reacting flows only. Their paper includes discussions of techniques with both implicit and explicit coupling between fluid and species equations. In addition, Molvik and Merkle[38] and Slomski *et al.*[39] describe fully implicit and implicit multigrid solution procedures, respectively, for chemically reacting flows. Both of these algorithms are based on extensions to the TVD upwind schemes of Osher and Chakravarthy[13–15]. Point relaxation is employed by Gnoffo *et al.* and Yee and Shinn for the solution of the associated large non-linear system of equations. This stratagem is computationally efficient because it does not necessitate the direct inversion of large block banded matrices. Molvik and Merkle use approximate factorization in conjunction with a modified Newton iteration technique in their solution procedure, whereas Slomski *et al.* employ approximate factorization in conjunction with a multigrid convergence acceleration procedure.

In other recent studies, Park and Yoon[40] have developed a fully coupled implicit algorithm that uses a flux-limited dissipation model to evaluate the higher-order numerical fluxes and a lower-upper factorization procedure that does not require the inversion of large banded matrices. As well, a comprehensive set of characteristic-based upwind techniques, that use either Runge–Kutta, implicit approximate-factorization, or implicit lower-upper decomposition time integration schemes are described by Walters *et al.*[41] for computing steady-state solutions of thermochemical non-equilibrium flows. In particular, their results emphasize the fact that explicit Runge–Kutta methods are generally inappropriate for non-equilibrium flow solution, at least for stationary flow applications.

This paper describes partially-decoupled semi-implicit and factored implicit TVD finite-difference schemes for the solution of the conservation laws governing two-dimensional non-equilibrium vibrationally relaxing and chemically reacting flows of thermally-perfect gaseous mixtures in a generalized transformed coordinate system. These schemes are variants of the techniques discussed above. In both the time-split semi-implicit and factored fully implicit methods, the gas-dynamic and thermodynamic equations are partially decoupled by employing a *frozen flow* approximation. The two sets of decoupled equations are then solved alternately in a lagged manner within a time marching procedure, thereby providing explicit coupling between the fluid conservation laws and the species concentration and vibrational energy equations. The semi-implicit formulation, based on Roe's higher-order TVD flux-difference split (FDS) scheme[7,8], is more appropriate for unsteady applications and the factored implicit form, based on Osher and Chakravarthy's high-resolution TVD schemes[13–15], is useful for obtaining steady-state solutions. An extension of Roe's approximate Riemann solver[7,18–20], giving the eigenvalues and eigenvectors of the fully coupled system, is used to evaluate the numerical flux functions in both FDS algorithms. Modifications to the Riemann solutions are also described

which ensure that physically realistic approximate solutions are obtained. The proposed partially-decoupled methods are shown to have several advantages over other chemistry-split and fully coupled techniques.

The presentation begins with a brief development of the conservation equations for two-dimensional non-equilibrium flows. This is followed by a description of the various aspects of the numerical algorithm, including details of the decoupling and flux-difference splitting procedures, time-stepping schemes, approximate Riemann solvers, and inviscid flux functions. Finally, some numerical predictions of non-stationary oblique shock-wave reflections and diffractions in both air and oxygen, as well as a blunt-body flow of nitrogen over a circular cylinder, are described in order to illustrate the capabilities of the techniques. Note that the inclusion of non-equilibrium finite-rate vibrational relaxation and chemical reaction effects in an efficient TVD solution algorithm is the present focus. Therefore, the study is restricted to two-dimensional planar inviscid flows. Extensions of the methods for application to three-dimensional viscous hypersonic flows are possible and are potential topics of future research.

CONSERVATION EQUATIONS

For the analysis described herein, it is assumed that the dynamic behaviour of the gaseous fluid of interest can be accurately represented by an inviscid continuum. This assumption is certainly valid for most inviscid flows with Knudsen numbers, Kn, less than 0.02[42]. (The Knudsen number is the ratio of the molecular mean free path to a characteristic length scale.) The thermodynamics of the continuum is modelled by treating it as a chemically reactive mixture of thermally perfect gases for which the thermal state can be described by a translational–rotational temperature and a set of vibrational temperatures (or energies), one for each polyatomic species. The translational–rotational temperature represents the contribution to the internal energy by the translational and rotational modes of all molecules and atoms in the mixture, which are assumed to be in thermal equilibrium. (This is a reasonable approximation for most continuum flows[43].) Each vibrational temperature represents the contribution to the internal energy by the vibrational modes of the corresponding polyatomic species. Intermolecular forces, electronic excitation, ionization rate, and radiation effects are all neglected.

Confining ourselves to two-dimensional planar flows, the weak conservation law forms of the mixture mass, momentum, and energy equations and the species mass and vibrational energy equations describing the inviscid non-stationary flow of a thermally perfect gaseous mixture may be written for a two-dimensional generalized curvilinear coordinate system as[42–45]:

$$\frac{\partial}{\partial t}(J\mathbf{U}) + \frac{\partial}{\partial \zeta}[\mathbf{F}(\mathbf{U})] + \frac{\partial}{\partial \eta}[\mathbf{G}(\mathbf{U})] = J\mathbf{S}(\mathbf{U}) \tag{1}$$

where the multi-component solution column vector $\mathbf{U}$ and source column vector $\mathbf{S}$ are given by:

$$\mathbf{U} = \begin{bmatrix} \rho \\ \rho u \\ \rho v \\ \rho[e + e_v + \frac{1}{2}(u^2 + v^2)] \\ \rho c_1 \\ \vdots \\ \rho c_N \\ \rho c_1 e_{v_1} \\ \vdots \\ \rho c_N e_{v_N} \end{bmatrix} \qquad \mathbf{S} = \begin{bmatrix} 0 \\ 0 \\ 0 \\ -\rho \sum_{s=1}^{N} w_s \Delta h^0_{f_s} \\ \rho w_1 \\ \vdots \\ \rho w_N \\ \rho c_1 q_1 + \rho \beta_1 w_1 e_{v_1} \\ \vdots \\ \rho c_N q_N + \rho \beta_N w_N e_{v_N} \end{bmatrix} \tag{2}$$

and the ζ- and η-direction flux column vectors $\mathbf{F}$ and $\mathbf{G}$ are:

$$\mathbf{F} = \begin{bmatrix} \rho U \\ \rho u U + y_\eta p \\ \rho v U - x_\eta p \\ \rho U\left[e + \dfrac{p}{\rho} + e_v + \dfrac{1}{2}(u^2 + v^2)\right] \\ \rho c_1 U \\ \vdots \\ \rho c_N U \\ \rho c_1 e_{v_1} U \\ \vdots \\ \rho c_N e_{v_N} U \end{bmatrix} \qquad \mathbf{G} = \begin{bmatrix} \rho V \\ \rho u V - y_\zeta p \\ \rho v V + x_\zeta p \\ \rho V\left[e + \dfrac{p}{\rho} + e_v + \dfrac{1}{2}(u^2 + v^2)\right] \\ \rho c_1 V \\ \vdots \\ \rho c_N V \\ \rho c_1 e_{v_1} V \\ \vdots \\ \rho c_N e_{v_N} V \end{bmatrix} \tag{3}$$

In (1)–(3), t is time, x and y are the Cartesian coordinates of the physical space, ρ is the mixture density, u and v are the velocity components in the physical coordinate system, p is the pressure, e is the total specific translational–rotational energy of the mixture, $c_s = \rho_s/\rho$ is the mass fraction of species s with $\sum_s c_s = 1$, ρ_s is the species density, e_{v_s} is the species vibrational energy, $e_v = \sum_s c_s e_{v_s}$ is the total specific vibrational energy of the mixture, and N is the number of species. The constant $\Delta h^0_{f_s}$ is the heat of formation of species s evaluated at a temperature of absolute zero (0 K) and the source term $-\rho \sum w_s \Delta h^0_{f_s}$ of (2) represents the total change in the zero-point energy of the mixture resulting from chemical reactions. Additionally, w_s is the time rate of change of the concentration of the species s brought about by the chemical reactions and q_s represents the time rate of change of the vibrational energy of the species s brought about by relaxation to its equilibrium value. The term $\rho \beta_s w_s e_{v_s}$ is related to the change in the vibrational energy of species s per unit volume of the mixture due to the chemical reactions. The parameter β_s is an empirical factor greater than or equal to unity and is used to reflect the observed preference of *higher-than-average* vibrationally excited molecules to dissociate and the tendency of atoms to combine and form higher-than-average vibrationally excited molecules[44]. Finally, ζ and η are the transformed coordinates, $x_\zeta = \partial x/\partial\zeta$, $x_\eta = \partial x/\partial\eta$, $y_\zeta = \partial y/\partial\zeta$, $y_\eta = \partial y/\partial\eta$ are the transformation metrics, and $J = x_\zeta y_\eta - x_\eta y_\zeta$ is the Jacobian of the coordinate transformation. $U = y_\eta u - x_\eta v$ and $V = x_\zeta v - y_\zeta u$ are the contravariant velocities. Note that the use of a curvilinear coordinate system facilitates complex boundary treatment and grid-point clustering in regions of large solution gradients.

Some additional thermodynamic relationships are useful. The pressure may be expressed in terms of the translational–rotational temperature T or energy e and the mixture properties by using the ideal equation of state for each thermally perfect species and applying Dalton's law of partial pressure. The resulting equation of state for the mixture is:

$$p = \rho R T = (\gamma - 1)\rho e \tag{4}$$

where $R = \mathscr{R}(\sum_s c_s/\mathscr{M}_s) = \sum_s c_s R_s$ is the specific gas constant of the mixture, $\mathscr{R}$ is the universal gas constant, $\mathscr{M}_s$ is the molecular weight of species s, $R_s = \mathscr{R}/\mathscr{M}_s$ is the specific gas constant of species s, and $\gamma = 1 + [\sum_s c_s R_s]/[\sum_s c_s R_s/(\gamma_s - 1)]$ is defined to be the *frozen* specific heat ratio of the mixture. The variable γ_s represents the frozen specific heat ratios of the species s. Note that these frozen specific heat ratios are the actual specific heat ratio of the species in the absence of vibrational excitation. It is also possible to define a frozen sound speed for the mixture. This intensive property may be related to the other mixture properties by:

$$a^2 = \gamma R T = \gamma \frac{p}{\rho} = \gamma(\gamma - 1)e \tag{5}$$

where a is the frozen sound speed.

Aside from the need for a more specific prescription of the source terms w_s and q_s, (1)–(5) provide a complete description of the inviscid flow of the non-equilibrium mixture in terms of a generalized two-dimensional curvilinear coordinate system.

NUMERICAL METHODS

Partially-decoupled approach

Time-marching upwind TVD finite-difference algorithms are now proposed for both non-stationary and stationary solutions of (1)–(3). However, rather than integrating this system of equations simultaneously in a directly coupled fashion, the hyperbolic conservation laws are first partially decoupled and two alternate subsystems are defined: a gas-dynamic and a thermodynamic subsystem. The resulting subsystems are then integrated sequentially in a two-stage time-lagged uncoupled manner. The form of the equation decoupling, subsequent flux-difference splitting approach, and formulation of these techniques within a TVD solution algorithm are new and are presented in full herein.

The decoupling procedure and associated time marching algorithm may be defined as follows. Given a solution $\mathbf{U}(\zeta, \eta, t_0)$ of (1) at time t_0, an approximate solution is obtained at some later time $t_0 + \Delta t$, where Δt is a small time increment, by first solving a gas-dynamic initial boundary value problem defined by:

$$\frac{\partial}{\partial t}(J\mathbf{W}) + \frac{\partial}{\partial \zeta}[\hat{\mathbf{F}}(\mathbf{W})] + \frac{\partial}{\partial \eta}[\hat{\mathbf{G}}(\mathbf{W})] = 0 \tag{6}$$

$$t_0 < t \leqslant t_0 + \Delta t, \qquad \mathbf{W}(\zeta, \eta, t_0) = \mathbf{W}(\mathbf{U}(\zeta, \eta, t_0)) \tag{7}$$

and then solving a non-equilibrium thermodynamic initial boundary value problem given by:

$$\frac{\partial}{\partial t}(J\mathbf{Q}) + U\frac{\partial}{\partial \zeta}[\mathbf{H}(\mathbf{Q})] + V\frac{\partial}{\partial \eta}[\mathbf{H}(\mathbf{Q})] = J\hat{\mathbf{S}}(\mathbf{Q}) \tag{8}$$

$$t_0 < t \leqslant t_0 + \Delta t, \qquad \mathbf{Q}(x, y, t_0) = \mathbf{Q}(\mathbf{W}(\zeta, \eta, t_0 + \Delta t), \mathbf{U}(\zeta, \eta, t_0)) \tag{9}$$

where the various solution, flux, and source column vectors of the two newly defined subsystems are:

$$\mathbf{W} = \begin{bmatrix} \rho \\ \rho u \\ \rho v \\ \rho\left[\dfrac{p}{\gamma - 1} + e_v + \dfrac{1}{2}(u^2 + v^2)\right] \\ \rho\gamma \\ \rho R \\ \rho e_v \end{bmatrix} \qquad \mathbf{Q} = \begin{bmatrix} c_1 \\ \vdots \\ c_N \\ c_1 e_{v_1} \\ \vdots \\ c_N e_{v_N} \\ \displaystyle\sum_{s=1}^{N}\left[\frac{c_s R_s}{(\gamma_s - 1)}T + c_s e_{v_s}\right] + \frac{1}{2}(u^2 + v^2) \end{bmatrix} \tag{10}$$

$$\hat{\mathbf{F}} = \begin{bmatrix} \rho U \\ \rho u U + y_\eta p \\ \rho v U - x_\eta p \\ \rho U\left[\dfrac{\gamma p}{(\gamma-1)\rho} + e_v + \dfrac{1}{2}(u^2+v^2)\right] \\ \rho U \gamma \\ \rho U R \\ \rho U e_v \end{bmatrix} \qquad \hat{\mathbf{G}} = \begin{bmatrix} \rho V \\ \rho u V - y_\zeta p \\ \rho v V + x_\zeta p \\ \rho V\left[\dfrac{\gamma p}{(\gamma-1)\rho} + e_v + \dfrac{1}{2}(u^2+v^2)\right] \\ \rho V \gamma \\ \rho V R \\ \rho V e_v \end{bmatrix} \tag{11}$$

$$\mathbf{H} = \begin{bmatrix} c_1 \\ \vdots \\ c_N \\ c_1 e_{v_1} \\ \vdots \\ c_N e_{v_N} \\ 0 \end{bmatrix} \qquad \hat{\mathbf{S}} = \begin{bmatrix} w_1 \\ \vdots \\ w_N \\ c_1 q_1 + \beta_1 w_1 e_{v_1} \\ \vdots \\ c_N q_N + \beta_N w_N e_{v_N} \\ -\sum_{s=1}^{N} w_s \Delta h^0_{f_s} \end{bmatrix} \tag{12}$$

The approximate solution at $t_0 + \Delta t$ is then given by:

$$\mathbf{U}(\zeta, \eta, t_0 + \Delta t) \approx \mathbf{U}(\mathbf{W}(\zeta, \eta, t_0 + \Delta t), \mathbf{Q}(\zeta, \eta, t_0 + \Delta t)) \tag{13}$$

A solution for all time $t > t_0$ may be obtained by repeating the two-step algorithm and, in the limit of vanishing Δt, this solution should converge to the exact solution of (1). Furthermore, as $t \to \infty$ a constant steady-state solution should be obtained.

The seven-component subsystem of (6) is derived by employing a *frozen flow* assumption and setting the finite-rate thermodynamic source terms of (1) to zero. These equations describe the non-equilibrium solution in the limit as the Damköhler number approaches zero. The behaviour of the mixture is essentially that of a thermally and calorically perfect gas, except that the specific heat ratio and gas constant may vary throughout the flow field and a portion of the internal energy is locked in the vibrational modes. The last three equations of the gas-dynamic subsystem are introduced to include these effects and describe changes in the quantities γ, R, and e_v, that, in the frozen flow limit, are merely convected with the flow. The use of separate flow equations for describing the evolution of these gas-dynamic quantities is akin to the ideas put forward by Colella and Glaz[17] for solving equilibrium flows of real gases. In their work, an equation for the convection of an *equivalent* γ was introduced for solving flows of real gases in complete thermodynamic equilibrium.

The multi-component N-species thermodynamic subsystem represented by (8) is derived by assuming that ρ, u, and v are known and fixed. It describes the time rate of change of the species mass fractions and vibrational energies and the total internal energy and includes the source terms neglected in the derivation of (6). The primitive variables c_s, e_{v_s}, and T, and consequently e, e_v, p and other thermodynamic properties are all updated by solving this subsystem.

Comparisons to chemistry-split and fully coupled methods

The preceding decoupling procedure is similar in spirit to the techniques put forward by Glaz *et al.*[29] and Ben-Artzi[30] and the resulting subsystems resemble, to some extent, the uncoupled equation sets that may be obtained by using the equation-partitioning procedure suggested by Yee and Shinn[33]. In the GRP method of Ben-Artzi for reactive flow, the solution of the homogeneous frozen-flow equations (i.e., source terms set to zero) is used to construct solutions for the fully reactive case. The basic proposition employed is that, for a given problem with initial conditions specified at $t = t_0$, the inhomogeneous solution can be equated to the homogeneous solution in the limit as $t \to t_0$ and that approximations to the reactive flow solution can be derived by applying corrections to the non-reacting solution. This is the essence of the present equation-decoupling technique.

The term 'partially decoupled' is applied here to distinguish the current method from fully coupled algorithms, which at each level in a marching procedure solve the complete set of conservation laws in a single step, and uncoupled, loosely coupled, or chemistry-split techniques, which at each level decouple the gas-dynamic and finite-rate thermodynamic equations and solve them separately in a two-stage process (see References 33 and 46). The partially-decoupled approach differs from uncoupled or chemistry-split methods because it provides a physically consistent procedure for separating the gas-dynamic and finite-rate models. Furthermore, it will be shown that the decoupling procedure readily permits the use of the eigenvalues and eigenvectors of the complete system in the evaluation of the numerical fluxes of each subsystem. Loosely coupled methods usually employ the eigenvalues and eigenvectors of each decoupled subsystem. The use of the eigenvalues and eigenvectors of the full equations should enhance the coupling between the equation sets and thereby improve numerical solution quality[33]. It can also be argued (see Reference 47 for details) that if the numerical solutions of (6) and (8) are constructed using the proposed approximate Riemann solvers and TVD schemes, then the approximate solutions preserve the monotonicity, positivity, and the maximum principles for the mass fractions of each species c_s as defined by Larrouturou[46], without requiring the solution of the fully coupled conservation laws. These principles ensure that $0 \leqslant c_s \leqslant 1$ and $\sum_s c_s = 1$, which are conditions that must be satisfied for physically realistic solutions. Larrouturou points out that chemistry-split and FDS fully coupled solution schemes do not always satisfy these important principles.

The primary advantages of the present decoupling procedure as compared to fully coupled methods are related to its simplicity and computational efficiency. One solver can be developed for the gas-dynamic subsystem of the partially-decoupled approach and used to predict the flow of many different non-equilibrium gaseous mixtures. Mixture-specific solvers are needed only for the thermodynamic subsystem. This simplifies computer program development and enhances algorithm versatility. Furthermore, with the partially-decoupled approach (as with chemistry-split methods), it is easy to employ local-time-stepping or subiteration procedures for solving the thermodynamic subsystem without changing the integration of the gas-dynamic subsystem. It is also easy to utilize different solvers for the thermodynamic subsystem in different regions of the flow depending on the solution characteristics. This additional capability makes the approach more flexible and may be useful for treating cases in which the source terms are very stiff[26].

The present decoupling technique can also lead to significant computational savings when fully implicit schemes are used to solve the gas-dynamic and thermodynamic subsystems. Although three additional equations must be solved for γ, R, and e_v, the reduced subsystems are of sizes 7 and $2N + 1$ as compared to the complete system that is of size $2N + 4$. In addition, it will be shown that for linearized factored implicit algorithms the solution of the inviscid thermodynamic subsystem does not require the inversion of full $(2N + 1) \times (2N + 1)$ block tridiagonal systems. In at least one sweep direction, it is only necessary to invert $2N$ scalar tridiagonal systems. In the other sweep direction, the submatrices of the off-diagonal blocks

contain only diagonal elements and simple diagonalization procedures are possible. For large systems, these features may be exploited to reduce the number of operation counts associated with each iteration of an implicit solution procedure.

In some cases, the explicit coupling of gas-dynamic and finite-rate subsystems provided by the present partial-decoupling procedure may not be adequate for numerical predictions of steady, viscous, combusting flows. Fully coupled algorithms with implicit coupling may be more efficient. However, for many applications like those considered in the next section, the partially-decoupled approach is valid and performs well. The technique has also been applied successfully by Groth *et al.*[48] to predict one-dimensional non-stationary non-equilibrium flow in a hypersonic impulse tunnel.

Eigensystems of flux Jacobian matrices

Having uncoupled the gas-dynamic and thermodynamic equations as described above, the two subsystems can be updated at each time level by means of a TVD finite-difference method. As TVD schemes were originally developed for solving linear and non-linear scalar homogeneous hyperbolic conservation laws in one space dimension, algorithm extensions are necessary for these weakly conservative two-dimensional subsystems. The non-linear and vector nature of the decoupled conservation laws is handled herein by adopting the characteristic decomposition or flux-difference splitting technique of Roe[7] in which the properties of the flux Jacobians are utilized in conjunction with approximate Riemann solvers to represent the solution and flux vector jumps in terms of characteristic variables. The homogeneous terms of the thermodynamic subsystem represent pure convection and the partial differential equations are therefore already in characteristic form. However, a decomposition procedure is required for the gas-dynamic subsystem. Following Glaister[18–20], extensions to Roe's approximate Riemann solver have been developed and are used in the evaluation of the numerical flux functions for (6) to account for the transformed coordinate system and the effects of varying γ and R and non-zero e_v. These approximate Riemann solutions require information about the eigensystems of the flux Jacobians $\hat{\mathbf{A}} = \partial\hat{\mathbf{F}}/\partial\mathbf{W}$ and $\hat{\mathbf{B}} = \partial\hat{\mathbf{G}}/\partial\mathbf{W}$.

It can be shown that the seven eigenvalues and right eigenvectors of the ζ-direction flux Jacobian satisfying $\hat{\mathbf{A}}\mathbf{e}_k = \lambda_k\mathbf{e}_k$, $k = 1, \ldots, 7$, are:

$$\lambda_1 = U - a\sqrt{x_\eta^2 + y_\eta^2}, \qquad \lambda_2 = \lambda_3 = \lambda_4 = \lambda_5 = \lambda_6 = y_\eta u - x_\eta v = U, \qquad \lambda_7 = U + a\sqrt{x_\eta^2 + y_\eta^2} \tag{14}$$

$$\mathbf{e}_1 = \begin{bmatrix} 1 \\ u - \dfrac{y_\eta a}{\sqrt{x_\eta^2 + y_\eta^2}} \\ v + \dfrac{x_\eta a}{\sqrt{x_\eta^2 + y_\eta^2}} \\ h - \dfrac{aU}{\sqrt{x_\eta^2 + y_\eta^2}} \\ \gamma \\ R \\ e_v \end{bmatrix}, \quad \mathbf{e}_2 = \begin{bmatrix} 1 \\ u \\ v \\ e_v + \frac{1}{2}(u^2 + v^2) \\ \gamma \\ R \\ e_v \end{bmatrix}, \quad \mathbf{e}_e = \begin{bmatrix} 0 \\ x_\eta \\ y_\eta \\ x_\eta u + y_\eta v \\ 0 \\ 0 \\ 0 \end{bmatrix} \tag{15}$$

$$\mathbf{e}_4 = \begin{bmatrix} 0 \\ 0 \\ 0 \\ \dfrac{-a^2}{(\gamma-1)^2} \\ \gamma \\ 0 \\ 0 \end{bmatrix}, \quad \mathbf{e}_5 = \begin{bmatrix} 0 \\ 0 \\ 0 \\ 0 \\ 0 \\ R \\ 0 \end{bmatrix}, \quad \mathbf{e}_6 = \begin{bmatrix} 0 \\ 0 \\ 0 \\ e_v \\ 0 \\ 0 \\ e_v \end{bmatrix}, \quad \mathbf{e}_7 = \begin{bmatrix} 1 \\ u + \dfrac{y_\eta a}{\sqrt{x_\eta^2 + y_\eta^2}} \\ v - \dfrac{x_\eta a}{\sqrt{x_\eta^2 + y_\eta^2}} \\ h + \dfrac{aU}{\sqrt{x_\eta^2 + y_\eta^2}} \\ \gamma \\ R \\ e_v \end{bmatrix} \tag{16}$$

where h is the specific enthalpy of the mixture and is given by:

$$h = e + \frac{p}{\rho} + e_v + \frac{1}{2}(u^2 + v^2) = \frac{\gamma p}{(\gamma - 1)\rho} + e_v + \frac{1}{2}(u^2 + v^2) \tag{17}$$

Similar expressions can be obtained for the flux Jacobian $\hat{\mathbf{B}}$ that satisfy $\hat{\mathbf{B}}\mathbf{e}_k = \lambda_k \mathbf{e}_k$. The eigenvalues and eigenvectors are:

$$\lambda_1 = V - a\sqrt{x_\zeta^2 + y_\zeta^2}, \quad \lambda_2 = \lambda_3 = \lambda_4 = \lambda_5 = \lambda_6 = x_\zeta v - y_\zeta u = V, \quad \lambda_7 = V + a\sqrt{x_\zeta^2 + y_\zeta^2} \tag{18}$$

$$\mathbf{e}_1 = \begin{bmatrix} 1 \\ u + \dfrac{y_\zeta a}{\sqrt{x_\zeta^2 + y_\zeta^2}} \\ v - \dfrac{x_\zeta a}{\sqrt{x_\zeta^2 + y_\zeta^2}} \\ h - \dfrac{aV}{\sqrt{x_\zeta^2 + y_\zeta^2}} \\ \gamma \\ R \\ e_v \end{bmatrix}, \quad \mathbf{e}_2 = \begin{bmatrix} 1 \\ u \\ v \\ e_v + \frac{1}{2}(u^2 + v^2) \\ \gamma \\ R \\ e_v \end{bmatrix}, \quad \mathbf{e}_3 = \begin{bmatrix} 0 \\ x_\zeta \\ y_\zeta \\ x_\zeta u + y_\zeta v \\ 0 \\ 0 \\ 0 \end{bmatrix} \tag{19}$$

$$\mathbf{e}_4 = \begin{bmatrix} 0 \\ 0 \\ 0 \\ \dfrac{-a^2}{(\gamma-1)^2} \\ \gamma \\ 0 \\ 0 \end{bmatrix}, \quad \mathbf{e}_5 = \begin{bmatrix} 0 \\ 0 \\ 0 \\ 0 \\ 0 \\ R \\ 0 \end{bmatrix}, \quad \mathbf{e}_6 = \begin{bmatrix} 0 \\ 0 \\ 0 \\ e_v \\ 0 \\ 0 \\ e_v \end{bmatrix}, \quad \mathbf{e}_7 = \begin{bmatrix} 1 \\ u - \dfrac{y_\zeta a}{\sqrt{x_\zeta^2 + y_\zeta^2}} \\ v + \dfrac{x_\zeta a}{\sqrt{x_\zeta^2 + y_\zeta^2}} \\ h + \dfrac{aV}{\sqrt{x_\zeta^2 + y_\zeta^2}} \\ \gamma \\ R \\ e_v \end{bmatrix} \tag{20}$$

Note that $\hat{\mathbf{A}}$ and $\hat{\mathbf{B}}$ each have only three distinct eigenvalues. The $k = 1$ and 7 characteristic fields of both matrices are genuinely non-linear in the sense of Lax (i.e., $\partial\lambda_k/\partial\mathbf{W}\cdot\mathbf{e}_k \neq 0$), whereas the $k = 2, 3, 4, 5$, and 6 eigenvalues and eigenvectors are linearly degenerate and are associated with purely convective fluxes. In addition, the unique eigenvalues of the gas-dynamic subsystem are identical to the unique eigenvalues of the fully coupled conservation laws of (1). This is exploited when constructing the approximate TVD solutions of the next subsections.

Semi-implicit TVD scheme

Using the proposed equation decoupling technique, finite-difference solutions of (1) can be obtained by solving the gas-dynamic and thermodynamic subsystems of (6) and (8) alternately in a time-lagged fashion. A semi-implicit TVD scheme is proposed for time-accurate numerical solutions. The implicit time differencing of source terms modelling the finite-rate processes effectively alleviates the stiffness associated with the relaxation and reaction time scales. The explicit treatment of the inviscid fluxes is generally quite efficient for unsteady applications. For the present study, the higher-order TVD upwind FDS scheme of Roe[7,8,49] is used as the underlying scalar solver. Like other TVD methods, the scheme is a *smart* solution adaptive method that provides improved numerical accuracy and monotonic or oscillation-free solutions by having difference coefficients which depend on the local solution at each time step. The *unlimited* constant-coefficient scheme is a combination of the second-order schemes of Lax and Wendroff[50] (central differences) and Warming and Beam[51] (upwind differences). Flux limiters (see Reference 49) are employed to limit the magnitude of the second-order antidiffusive fluxes and reduce the scheme to the first-order fully-upwind method of Cole and Murman[52] at local extrema of the solution. The extension to two dimensions is achieved by the usual Strang-splitting or operator-splitting method[53,54], in which the one-dimensional algorithm is applied to the one-dimensional analogues of the multi-dimensional equation sets in both coordinate directions. Approximate Riemann solvers are employed to decompose solution and flux vectors of the time-split conservation laws, which are then solved by applying explicit and semi-implicit versions of Roe's scheme to each characteristic field in a *scalar* fashion.

As with other TVD schemes, the term 'higher-order' is applied to Roe's method to indicate that the formal spatial accuracy of the scheme with a uniform computational mesh is second-order in regions where the solution is smooth (i.e., almost everywhere), but reduces to first-order at extrema. In the case of linear and non-linear scalar homogeneous hyperbolic conservation laws and linear systems of homogeneous conservation laws in one space dimension, the resulting *non-linear* scheme is TVD[5,6], which guarantees that the solutions are also monotonicity preserving. In the more general case of non-linear multidimensional systems, the accuracy and TVD properties may not be realized. First, the truncation error in the physical space can be achieved only when the coordinate transformation is smooth[55]. Furthermore, the notion of what constitutes a TVD solution in two space dimensions remains largely unresolved. Goodman and LeVeque[56] argue that time-split TVD algorithms applied to two-dimensional systems are, at most, first-order accurate. However, the recent work of Colella[54] indicates that operator split methods have the same resolution as unsplit methods and many other numerical experiments indicate that higher-order TVD techniques afford improved solution accuracy.

The proposed semi-implicit algorithm can be formulated as follows. Let $\mathbf{U}_{i,j}^n$ be the numerical approximation of the solution of (1) at time $t = t^n$ and at discrete locations (i, j), with curvilinear coordinates (ζ_i, η_j). The numerical solution at subsequent time levels is obtained by means of the fully-discrete time-stepping procedure:

$$\mathbf{U}_{i,j}^{n+2} = \mathscr{L}_{Q_\eta}^{\Delta t/2}\,\mathscr{L}_{Q_\zeta}^{\Delta t/2}\,\mathscr{L}_{W_\eta}^{\Delta t}\,\mathscr{L}_{W_\zeta}^{\Delta t}\,\mathscr{L}_{W_\eta}^{\Delta t/2}\,\mathscr{L}_{Q_\zeta}^{\Delta t/2}\,\mathscr{L}_{Q_\eta}^{\Delta t/2}\,\mathbf{U}_{i,j}^n \tag{21}$$

with $\Delta t^n = t^{n+1} - t^n$, and where the gas-dynamic and thermodynamic subsystem solution

operators are:

$$\mathscr{L}^{\Delta t}_{W_\zeta}\mathbf{U}^n_{i,j} = \mathbf{U}(\widehat{\mathbf{W}^{n+1}_{i,j}}, \mathbf{Q}^n_{i,j})\colon \Delta\mathbf{W}^{\hat{n}}_{i,j} = \widehat{\mathbf{W}^{n+1}_{i,j}} - \mathbf{W}^n_{i,j} = -\frac{\Delta t^n}{J_{i,j}\Delta\zeta_{i,j}}[\hat{\mathscr{F}}^n_{i+1/2,j} - \hat{\mathscr{F}}^n_{i-1/2,j}] \quad (22)$$

$$\mathscr{L}^{\Delta t}_{W_\eta}\mathbf{U}^n_{i,j} = \mathbf{U}(\widehat{\mathbf{W}^{n+1}_{i,j}}, \mathbf{Q}^n_{i,j})\colon \Delta\mathbf{W}^{\hat{n}}_{i,j} = \widehat{\mathbf{W}^{n+1}_{i,j}} - \mathbf{W}^n_{i,j} = -\frac{\Delta t^n}{J_{i,j}\Delta\eta_{i,j}}[\hat{\mathscr{G}}^n_{i,j+1/2} - \hat{\mathscr{G}}^n_{i,j-1/2}] \quad (23)$$

$$\mathscr{L}^{\Delta t}_{Q_\zeta}\mathbf{U}^n_{i,j} = \mathbf{U}(\mathbf{W}^n_{i,j}, \widehat{\mathbf{Q}^{n+1}_{i,j}})\colon \left[\mathbf{I} - \Theta\Delta t^n\left(\frac{\partial\hat{\mathbf{S}}}{\partial\mathbf{Q}}\right)^n_{i,j}\right]\Delta\mathbf{Q}^{\hat{n}}_{i,j}$$

$$= \Delta t^n\hat{\mathbf{S}}^n_{i,j} - \frac{\Delta t^n U^n_{i,j}}{J_{i,j}\Delta\zeta_{i,j}}[\mathscr{H}^n_{i+1/2,j} - \mathscr{H}^n_{i-1/2,j}] \quad (24)$$

$$\mathscr{L}^{\Delta t}_{Q_\eta}\mathbf{U}^n_{i,j} = \mathbf{U}(\mathbf{W}^n_{i,j}, \widehat{\mathbf{Q}^{n+1}_{i,j}})\colon \Delta\mathbf{Q}^{\hat{n}}_{i,j} = \widehat{\mathbf{Q}^{n+1}_{i,j}} - \mathbf{Q}^n_{i,j} = -\frac{\Delta t^n V^n_{i,j}}{J_{i,j}\Delta\eta_{i,j}}[\mathscr{H}^n_{i,j+1/2} - \mathscr{H}^n_{i,j-1/2}] \quad (25)$$

In the preceding equations, $\Delta\mathbf{W}^{\hat{n}}_{i,j} = \widehat{\mathbf{W}^{n+1}_{i,j}} - \mathbf{W}^n_{i,j}$, $\Delta\mathbf{Q}^{\hat{n}}_{i,j} = \widehat{\mathbf{Q}^{n+1}_{i,j}} - \mathbf{Q}^n_{i,j}$, and $\widehat{\mathbf{W}^{n+1}_{i,j}}$ and $\widehat{\mathbf{Q}^{n+1}_{i,j}}$ denote intermediate solution states and $\hat{\mathscr{F}}^n_{i+1/2,j}$, $\hat{\mathscr{G}}^n_{i,j+1/2}$, $\mathscr{H}^n_{i+1/2,j}$, and $\mathscr{H}^n_{i,j+1/2}$ are numerical approximations to the flux functions $\hat{\mathbf{F}}$, $\hat{\mathbf{G}}$, and $\mathbf{H}$, respectively, evaluated at time level n and nodal interfaces $(i+1/2, j)$ and $(i, j+1/2)$. In (24), $\mathbf{I}$ is the identity matrix, $\partial\hat{\mathbf{S}}/\partial\mathbf{Q}$ is the source Jacobian matrix, and the term $[\mathbf{I} - \Theta\Delta t^n(\partial\hat{\mathbf{S}}/\partial\mathbf{Q})^n_{i,j}]$ is similar to the preconditioning matrices used by Bussing and Murman[34]. The parameter Θ controls the time integration of the source terms of the operator $\mathscr{L}^{\Delta t}_{Q_\zeta}$. For $\Theta = 0$, the time differencing is Euler explicit. For $\Theta = 1$, the time differencing is Euler implicit. This value produces the most stable scheme and is appropriate for problems with extremely stiff source terms. A value of $\Theta = 1/2$ produces a trapezoidal implicit time differencing that is best suited and consistent with the explicit time-differencing of the homogeneous terms.

The numerical flux functions for the gas-dynamic subsystem spatial operator $\mathscr{L}^{\Delta t}_{W_\zeta}$ are evaluated as follows:

$$\frac{\Delta t^n}{J_{i,j}\Delta\zeta_{i,j}}[\hat{\mathscr{F}}^n_{i+1/2,j} - \hat{\mathscr{F}}^n_{i-1/2,j}]$$

$$= \frac{1}{2}\sum_{k=1}^{7}\{[(\nu^n_{i+1/2,j,k} - |\nu^n_{i+1/2,j,k}|) + \phi^n_{i+1/2,j,k}|\nu^n_{i+1/2,j,k}|(1 - |\nu^n_{i+1/2,j,k}|)]\Delta\mathbf{W}^n_{i+1/2,j,k}$$

$$+ [(\nu^n_{i-1/2,j,k} + |\nu^n_{i-1/2,j,k}|) - \phi^n_{i-1/2,j,k}|\nu^n_{i-1/2,j,k}|(1 - |\nu^n_{i-1/2,j,k}|)]\Delta\mathbf{W}^n_{i-1/2,j,k}\} \quad (26)$$

where the quantities $\nu^n_{i+1/2,j,k}$, $\Delta\mathbf{W}^n_{i+1/2,j,k}$, and $\phi^n_{i+1/2,j,k}$ are the local average Courant–Friedrichs–Lewy (CFL) number, solution jump vector, and flux limiter for the kth elemental wave of the spatial operator, respectively. Note that, in this case, there are a total of seven elemental waves. The CFL numbers and solutions jump vectors are given by:

$$\nu^n_{i+1/2,j,k} = \frac{\Delta t^n\lambda^n_{i+1/2,j,k}}{J_{i+1/2,j}\Delta\zeta_{i+1/2,j}}, \qquad \Delta\mathbf{W}^n_{i+1/2,j,k} = \alpha^n_{i+1/2,j,k}\mathbf{e}^n_{i+1/2,j,k} \quad (27)$$

where $\Delta\zeta_{i+1/2,j} = \zeta_{i+1,j} - \zeta_{i,j}$, and there the required transformation metrics $x_{\eta_{i+1/2,j}}$, $y_{\eta_{i+1/2,j}}$, $x_{\zeta_{i+1/2,j}}$, and $y_{\zeta_{i+1/2,j}}$ and Jacobian $J_{i+1/2,j}$ may be approximated by standard second-order central finite-difference relations. In (27), $\lambda^n_{i+1/2,j,k}$ and $\mathbf{e}^n_{i+1/2,j,k}$ are the kth eigenvalue and eigenvector of the ζ-direction gas-dynamic flux Jacobian $\hat{\mathbf{A}}$ evaluated at an appropriate average state $\mathbf{W}^n_{i+1/2,j,k}$. They are defined by $\lambda^n_{i+1/2,j,k} = \lambda_k(\mathbf{W}^n_{i+1/2,j,k})$ and $\mathbf{e}^n_{i+1/2,j,k} = \mathbf{e}_k(\mathbf{W}^n_{i+1/2,j,k})$ where λ_k and $\mathbf{e}_k$ are given by (14)–(16). Here, $\alpha^n_{i+1/2,j,k}$ are defined to be the elemental or characteristic wave strengths which are also evaluated at the average state $\mathbf{W}^n_{i+1/2,j,k}$. An extension of Roe's approximate Riemann problem solution for the subsystem of (6), derived for the present work,

yields appropriate expressions for the wave strengths and various dependent variables defining the average state. The wave strengths of the $\mathscr{L}^{\Delta t}_{W_\xi}$ spatial operator satisfying the conditions $\Delta \mathbf{W}^n_{i+1/2,j} = \mathbf{W}^n_{i+1,j} - \mathbf{W}^n_{i,j} = \sum_k \Delta \mathbf{W}^n_{i+1/2,j,k} = \sum_k \alpha^n_{i+1/2,j,k}\mathbf{e}^n_{i+1/2,j,k}$ and $\Delta \hat{\mathbf{F}}^n_{i+1/2,j} = \hat{\mathbf{F}}^n_{i+1,j} - \hat{\mathbf{F}}^n_{i,j} = \sum_k \lambda^n_{i+1/2,j,k}\Delta \mathbf{W}^n_{i+1/2,j,k}$ are:

$$\alpha^n_{i+1/2,j,1} = \frac{1}{2(a^n_{i+1/2,j})^2}\left[\Delta p^n_{i+1/2,j} - \rho^n_{i+1/2,j}a^n_{i+1/2,j}\frac{y_{\eta_{i+1/2,j}}\Delta u^n_{i+1/2,j} - x_{\eta_{i+1/2,j}}\Delta v^n_{i+1/2,j}}{\sqrt{x^2_{\eta_{i+1/2,j}} + y^2_{\eta_{i+1/2,j}}}}\right] \tag{28}$$

$$\alpha^n_{i+1/2,j,2} = \Delta \rho^n_{i+1/2,j} - \frac{\Delta p^n_{i+1/2,j}}{(a^n_{i+1/2,j})^2}, \qquad \alpha^n_{i+1/2,j,3} = \rho^n_{i+1/2,j}\frac{x_{\eta_{i+1/2,j}}\Delta u^n_{i+1/2,j} + y_{\eta_{i+1/2,j}}\Delta v^n_{i+1/2,j}}{x^2_{\eta_{i+1/2,j}} + y^2_{\eta_{i+1/2,j}}} \tag{29}$$

$$\alpha^n_{i+1/2,j,4} = \frac{\rho^n_{i+1/2,j}}{\gamma^n_{i+1/2,j}}\Delta \gamma^n_{i+1/2,j}, \quad \alpha^n_{i+1/2,j,5} = \frac{\rho^n_{i+1/2,j}}{R^n_{i+1/2,j}}\Delta R^n_{i+1/2,j}, \quad \alpha^n_{i+1/2,j,6} = \frac{\rho^n_{i+1/2,j}}{e^n_{v_{i+1/2,j}}}\Delta e^n_{v_{i+1/2,j}} \tag{30}$$

$$\alpha^n_{i+1/2,j,7} = \frac{1}{2(a^n_{i+1/2,j})^2}\left[\Delta p^n_{i+1/2,j} + \rho^n_{i+1/2,j}a^n_{i+1/2,j}\frac{y_{\eta_{i+1/2,j}}\Delta u^n_{i+1/2,j} - x_{\eta_{i+1/2,j}}\Delta v^n_{i+1/2,j}}{\sqrt{x^2_{\eta_{i+1/2,j}} + y^2_{\eta_{i+1/2,j}}}}\right] \tag{31}$$

and

$$\rho^n_{i+1/2,j} = \sqrt{\rho^n_{i+1,j}\rho^n_{i,j}}, \; Z^n_{i+1/2,j} = \frac{\sqrt{\rho^n_{i+1,j}}Z^n_{i+1,j} + \sqrt{\rho^n_{i,j}}Z^n_{i,j}}{\sqrt{\rho^n_{i+1,j}} + \sqrt{\rho^n_{i,j}}}, \; Z = u, v, \gamma, R, e_v \text{ and } h \tag{32}$$

$$(a^n_{i+1/2,j})^2 = (\gamma^n_{i+1/2,j} - 1)[h^n_{i+1/2,j} - e^n_{v_{i+1/2,j}} - \frac{1}{2}\{(u^n_{i+1/2,j})^2 + (v^n_{i+1/2,j})^2\}] \tag{33}$$

are approximate Roe averages of the primitive variables defining $\mathbf{W}^n_{i+1/2,j,k}$. Note that for (28)–(31), the notation $\Delta Z^n_{i+1/2,j} = Z^n_{i+1,j} - Z^n_{i,j}$ and $\Delta Z^n_{i,j+1/2} = Z^n_{i,j+1} - Z^n_{i,j}$ is assumed. A similar set of equations is used to evaluate the numerical flux functions for the gas-dynamic subsystem spatial operator $\mathscr{L}^{\Delta t}_{W_\eta}$.

The flux functions of the $N_D = 2N + 1$ component thermodynamic subsystem have slightly different forms. The discrete difference expression:

$$\begin{aligned}\frac{\Delta t^n U^n_{i,j}}{J_{i,j}\Delta \zeta_{i,j}}[\mathscr{H}^n_{i+1/2,j} - \mathscr{H}^n_{i-1/2,j}] = \frac{1}{2}\sum_{k=1}^{2N+1}\{&[(\omega^n_{i+1/2,j} - |\omega^n_{i+1/2,j}|)\\ &+ \psi^n_{i+1/2,j,k}|\omega^n_{i+1/2,j}|(1 - |\omega^n_{i+1/2,j}|)]\Delta \mathbf{H}^n_{i+1/2,j,k}\\ &+ [(\omega^n_{i-1/2,j} + |\omega^n_{i-1/2,j}|)\\ &- \psi^n_{i-1/2,j,k}|\omega^n_{i-1/2,j}|(1 - |\omega^n_{i-1/2,j}|)]\Delta \mathbf{H}^n_{i-1/2,j,k}\}\end{aligned} \tag{34}$$

is used for the convective terms of the ζ-direction spatial operator $\mathscr{L}^{\Delta t}_{Q_\zeta}$, where $\omega^n_{i+1/2,j}$ is the local CFL number, $\Delta \mathbf{H}^n_{i+1/2,j,k}$ is the species concentration and vibrational energy jump column vector, and $\psi^n_{i+1/2,j,k}$ is the associated flux limiter. In (34), the CFL numbers and jump column vectors are prescribed by:

$$\omega^n_{i+1/2,j} = \frac{\Delta t^n U^n_{i+1/2,j}}{J_{i+1/2,j}\Delta \zeta_{i+1/2,j}} \qquad \Delta \mathbf{H}^n_{i+1/2,j,k} = \mathbf{D}_k \Delta \mathbf{H}^n_{i+1/2,j} \tag{35}$$

where $U^n_{i+1/2,j}$ is the local average convection velocity, $\Delta \mathbf{H}^n_{i+1/2,j} = \mathbf{H}^n_{i+1,j} - \mathbf{H}^n_{i,j}$, $\mathbf{D}_k$ is a diagonal matrix for which the elements of the diagonal are $(\delta_{1k}, \ldots, \delta_{kk}, \ldots, \delta_{N_D k})$, and δ is the usual Kronecker delta function. Here, the average convection velocity is determined by using the eigenvalue associated with the linear fields of the gas-dynamic subsystem and is specified as follows: $U^n_{i+1/2,j} = \lambda^n_{i+1/2,j,2}$ (and $V^n_{i,j+1/2} = \lambda^n_{i,j+1/2,2}$). In this way the eigenvalues of the fully coupled system are used in the computation of the flux functions of both the gas-dynamic and

thermodynamic subsystems. A very similar evaluation procedure is adopted for the flux functions of the $\mathscr{L}_{Q_\eta}^{\Delta t}$ solution operator.

The flux limiters $\phi^n_{i+1/2,j,k}$ and $\psi^n_{i+1/2,j,k}$ appearing in (26) and (34) for the ζ-sweep operators are defined to be functions of the local antidiffusive flux ratios and the local CFL numbers. They are determined by:

$$\phi^n_{i+1/2,j,k} = \sigma^{+n}_{i+1/2,j,k}\varphi_k(b^n_{i+1/2,j,k}) + \sigma^{-n}_{i+1/2,j,k}\varphi_k(1/b^n_{i+3/2,j,k}) \tag{36}$$

$$\psi^n_{i+1/2,j,k} = \tilde{\sigma}^{+n}_{i+1/2,j}\varphi_k(\tilde{b}^n_{i+1/2,j,k}) + \tilde{\sigma}^{-n}_{i+1/2,j}\varphi_k(1/\tilde{b}^n_{i+3/2,j,k}) \tag{37}$$

where $\varphi_k = \varphi_k(b)$ is the flux limiter function for the kth characteristic field, $\sigma^{\pm n}_{i+1/2,j,k} = (\sigma^n_{i+1/2,j,k} \pm 1)/2$, and $\sigma^n_{i+1/2,j,k}$ is the sign of $\lambda^n_{i+1/2,j,k}$ and equal to $+1$ if $\lambda^n_{i+1/2,j,k}$ is positive and -1 otherwise. Equivalently, $\tilde{\sigma}^{\pm n}_{i+1/2,j} = (\tilde{\sigma}^n_{i+1/2,j} \pm 1)/2$, and $\tilde{\sigma}^n_{i+1/2,j}$ is the sign of $\omega^n_{i+1/2,j}$. The flux ratios $b^n_{i+1/2,j,k}$ and $\tilde{b}^n_{i+1/2,j,k}$ for the gas-dynamic and thermodynamic subsystems are defined by the ratio of the antidiffusive fluxes:

$$b^n_{i+1/2,j,k} = \frac{|v^n_{i-1/2,j,k}|(1 - |v^n_{i-1/2,j,k}|)(\Delta \mathbf{W}^n_{i-1/2,j,k}\cdot \mathbf{N}_{w_k})}{|v^n_{i+1/2,j,k}|(1 + |v^n_{i+1/2,j,k}|)(\Delta \mathbf{W}^n_{i+1/2,j,k}\cdot \mathbf{N}_{w_k})} \tag{38}$$

$$\tilde{b}^n_{i+1/2,j,k} = \frac{|\omega^n_{i-1/2,j}|(1 - |\omega^n_{i-1/2,j}|)(\Delta \mathbf{H}^n_{i-1/2,j,k}\cdot \mathbf{N}_{H_k})}{|\omega^n_{i+1/2,j}|(1 - |\omega^n_{i+1/2,j}|)(\Delta \mathbf{H}^n_{i+1/2,j,k}\cdot \mathbf{N}_{H_k})} \tag{39}$$

where $\mathbf{N}_{W_k}$ and $\mathbf{N}_{H_k}$ are normalization row vectors. In the present algorithm, $\mathbf{N}_{W_k} = [1, 0, 0, 0, 0, 0, 0]$ for $k = 1$, 2, and 7, and $\mathbf{N}_{W_3} = [0, 0, 0, 1, 0, 0, 0]$, $\mathbf{N}_{W_4} = [0, 0, 0, 0, 1, 0, 0]$, $\mathbf{N}_{W_5} = [0, 0, 0, 0, 0, 1, 0]$, and $\mathbf{N}_{W_6} = [0, 0, 0, 0, 0, 0, 1]$, and $\mathbf{N}_{H_k}$ is chosen to recover the component of the antidiffusive flux vector associated with the kth component of the solution vector $\mathbf{Q}$. Following Sweby[49], various combinations of flux limiter functions φ_k are used for each of the characteristic fields. Three different functions are employed in the present algorithm. They are the well-known *minmod* limiter, van Leer's flux limiter, and the *superbee* limiter of Roe given by:

$$\varphi_k(b) = \max(0, \min(1, b)), \qquad \varphi_k(b) = \max\left(0, \frac{2b}{1+b}\right), \qquad \varphi_k(b) = \max(0, \min(1, 2b), \min(2, b)) \tag{40}$$

respectively. The latter more compressive limiter improves the sharpness of contact surfaces and slip streams. Similar flux-limiter formulations are used for the η-direction solution operators.

Finally, it should be noted that it is necessary to modify Roe's scheme near sonic points in order that the method be entropy satisfying and converge to the correct physical solution. In particular, the flux functions associated with non-linear characteristic fields 1 and 7 of the spatial operators $\mathscr{L}_{W_\xi}^{\Delta t}$ and $\mathscr{L}_{W_\eta}^{\Delta t}$ must be augmented to prevent the formation of aphysical *expansion* shocks. A variant of the entropy fix suggested by Roe and Pike[8] is employed. Consider elemental wave 1 of the operator $\mathscr{L}_{W_\xi}^{\Delta t}$. A wave spreading parameter for this wave is defined to be:

$$\delta^n_{i+1/2,j,1} = 2[\lambda^n_{i+1/2,j,1} - (U^n_{i,j} - a^n_{i,j}\sqrt{x^2_{\eta_{i+1/2,j}} + y^2_{\eta_{i+1/2,j}}})] \tag{41}$$

If $\lambda^n_{i+1/2,j,1} - 1/2\delta^n_{i+1/2,j,1} < 0$ and $\lambda^n_{i+1/2,j,1} + 1/2\delta^n_{i+1/2,j,1} > 0$, then the flux limiter $\phi^n_{i+1/2,j,1}$ is set to zero and the first-order flux jump is split into two components, that is,

$$\tfrac{1}{2}(v^n_{i+1/2,j,1} - |v^n_{i+1/2,j,1}|)\Delta \mathbf{W}^n_{i+1/2,j,1} \tag{42}$$

is replaced by:

$$\frac{1}{2}(v^{n+}_{i+1/2,j,1} - |v^{n+}_{i+1/2,j,1}|)\Delta \mathbf{W}^n_{i+1/2,j,1} + \tfrac{1}{2}(v^{n-}_{i+1/2,j,1} - |v^{n-}_{i+1/2,j,1}|)\Delta \mathbf{W}^n_{i+1/2,j,1} \tag{43}$$

where

$$v^{n+}_{i+1/2,j,1} = (\lambda^n_{i+1/2,j,1} + \tfrac{1}{2}\delta^n_{i+1/2,j,1}), \qquad v^{n-}_{i+1/2,j,1} = (\lambda^n_{i+1/2,j,1} - \tfrac{1}{2}\delta^n_{i+1/2,j,1}) \tag{44}$$

Equivalent procedures are required for the other non-linear characteristic fields.

The complete semi-implicit time-marching procedure represented by (21) is conditionally stable. The CFL criterion:

$$\Delta t^n < C_{\mathrm{CFL}} \min_{i,j} \left(\frac{J\Delta\zeta}{|U| + a\sqrt{x_\eta^2 + y_\eta^2}}, \frac{J\Delta\eta}{|V| + a\sqrt{x_\zeta^2 + y_\zeta^2}} \right) \tag{45}$$

is used to restrict the magnitude of the time increment and thereby ensure stability and convergence of the numerical solution for $\Theta \geqslant 1/2$. In (45), C_{CFL} is a positive valued constant in the range $0 < C_{\mathrm{CFL}} < 1$.

For very stiff cases, the time step imposed by (45) can be much larger than the fastest time scales associated with the finite-rate source terms. Although the present semi-implicit algorithm remains stable, this may result in the loss of accuracy in predicted non-equilibrium shock-front structure. For many applications, this form of solution degradation is not too detrimental as the computed jump conditions and propagation speeds of the discontinuities should still be physically correct, provided that the spatial resolution of the grid is sufficient. If more accurate resolution of relaxation fronts are required, then smaller time increments will improve the situation; however, it should be emphasized that spatial resolution is as important as temporal resolution. LeVeque and Yee[26] and Griffiths *et al.*[27] have studied the construction of numerical solutions for a model scalar advection equation with a non-linear source term. Both fully coupled and split solution algorithms were considered. For very stiff problems, they have shown that, in some cases, the schemes produce incorrect propagation speeds for discontinuities and that these wave propagation errors result from a lack of spatial resolution. In particular, Griffiths *et al.* have contrasted coupled explicit monotone and (chemistry) split schemes and have shown that, with increasing stiffness, the solutions of the split schemes remain monotone and bounded but the predicted or numerical propagation speeds do not coincide with the actual or true wave speeds. They have also shown that the coupled schemes diverge with increasing stiffness. Numerical computations of one-dimensional shock wave propagation problems in air were performed as part of the present study using the proposed semi-implicit method. Although these results will not be presented, they confirm the observations of LeVeque and Yee and indicate that care must be exercised in selecting the spatial mesh to ensure that discontinuities are sufficiently resolved. It is felt that further study of the effects of stiffness is warranted.

Fully implicit TVD scheme

A factored fully implicit scheme is also proposed for the solution of (1) via the partially-decoupled approach and the time integration of (6) and (8). This scheme is more suitable for steady-state applications. The basic solution approach follows those given by Chakravarthy[57] for perfect gases. The numerical flux functions of both the gas-dynamic and thermodynamic subsystems are evaluated by applying the flux-difference splitting technique used in the preceding semi-implicit scheme in conjunction with the one-parameter family of higher-order TVD upwind methods devised by Osher and Chakravarthy[13–15] as the underlying scalar schemes. The spatial discretization is coupled to a one-step one-parameter implicit time discretization. A factored non-conservative linearization procedure is employed for the implicit operators in which only the first-order terms of the spatial discretization are considered and the Roe-average state, eigenvalues, and eigenvectors of the flux Jacobians are assumed to be slowly varying functions of the solution vectors and are thus treated as locally constant. The factorization of the implicit operators avoids the inversion of very large matrices. The first-order linearization technique has the disadvantage that time accuracy is essentially lost because the implicit operators

are not conservative and the implicit and explicit operators no longer possess the same spatial accuracy. However, the underlying scheme can be shown to be TVD and has the advantage that it is simple and efficient to implement. Additionally, by including the higher-order terms in the explicit operators, steady-state solutions will possess the high-accuracy features and required conservation properties.

The two-parameter partially-decoupled factored fully implicit scheme can be expressed as:

$$\mathbf{U}_{i,j}^{n+1} = \mathscr{L}_Q^{\Delta t}\mathscr{L}_W^{\Delta t}\mathbf{U}_{i,j}^n \tag{46}$$

where $\mathscr{L}_W^{\Delta t}\mathbf{U}_{i,j}^n = \mathbf{U}(\widehat{\mathbf{W}_{i,j}^{n+1}}, \mathbf{Q}_{i,j}^n)$ and the fully-discrete gas-dynamic solution operator $\mathscr{L}_W^{\Delta t}$ is:

$$\left[\Theta\sum_{k=1}^{7}(\nu_{i,j+1/2,k}^{-n}\mathbf{e}_{i,j+1/2,k}^{n}\mathbf{A}_{i,j+1/2,k}^{-n})\right]\Delta\mathbf{W}_{i,j+1}^{\hat{n}} + \left[\Theta\sum_{k=1}^{7}(\nu_{i,j-1/2,k}^{+n}\mathbf{e}_{i,j-1/2,k}^{n}\mathbf{C}_{i,j-1/2,k}^{+n})\right]\Delta\mathbf{W}_{i,j-1}^{\hat{n}}$$
$$+\left[\mathbf{I}+\Theta\sum_{k=1}^{7}(\nu_{i,j+1/2,k}^{-n}\mathbf{e}_{i,j+1/2,k}^{n}\mathbf{B}_{i,j+1/2,k}^{-n}+\nu_{i,j-1/2,k}^{+n}\mathbf{e}_{i,j-1/2,k}^{n}\mathbf{B}_{i,j-1/2,k}^{+n})\right]\Delta\mathbf{W}_{i,j}^{\hat{n}}$$
$$=-\frac{\Delta t^n}{J_{i,j}\Delta\zeta_{i,j}}[\hat{\mathscr{F}}_{i+1/2,j}^{n}-\hat{\mathscr{F}}_{i-1/2,j}^{n}]-\frac{\Delta t^n}{J_{i,j}\Delta\eta_{i,j}}[\hat{\mathscr{G}}_{i,j+1/2}^{n}-\hat{\mathscr{G}}_{i,j-1/2,j}^{n}] \tag{47}$$

$$\left[\Theta\sum_{k=1}^{7}(\nu_{i+1/2,j,k}^{-n}\mathbf{e}_{i+1/2,j,k}^{n}\mathbf{A}_{i+1/2,j,k}^{-n})\right]\Delta\mathbf{W}_{i+1,j}^{\hat{n}} + \left[\Theta\sum_{k=1}^{7}(\nu_{i-1/2,j,k}^{+n}\mathbf{e}_{i-1/2,j,k}^{n}\mathbf{C}_{i-1/2,j,k}^{+n})\right]\Delta\mathbf{W}_{i-1,j}^{\hat{n}}$$
$$+\left[\mathbf{I}+\Theta\sum_{k=1}^{7}(\nu_{i+1/2,j,k}^{-n}\mathbf{e}_{i+1/2,j,k}^{n}\mathbf{B}_{i+1/2,j,k}^{-n}+\nu_{i-1/2,j,k}^{+n}\mathbf{e}_{i-1/2,j,k}^{n}\mathbf{B}_{i-1/2,j,k}^{+n})\right]\Delta\mathbf{W}_{i,j}^{\hat{n}}=\Delta\mathbf{W}_{i,j}^{\bar{n}} \tag{48}$$

$$\mathbf{W}_{i,j}^{\hat{n}} = \mathbf{W}_{i,j}^{n} + \Delta\mathbf{W}_{i,j}^{\hat{n}} \tag{49}$$

and where $\mathscr{L}_Q^{\Delta t}\mathbf{U}_{i,j}^n = \mathbf{U}(\mathbf{W}_{i,j}^n, \widehat{\mathbf{Q}_{i,j}^{n+1}})$ and the thermodynamic solution operator $\mathscr{L}_Q^{\Delta t}$ is:

$$\Theta\omega_{i,j+1/2}^{-n}\mathbf{D}_N\Delta\mathbf{Q}_{i,j+1}^{\bar{n}} - \Theta\omega_{i,j-1/2}^{+n}\mathbf{D}_N\Delta\mathbf{Q}_{i,j-1}^{\bar{n}} + [\mathbf{I}-\Theta(\omega_{i,j+1/2}^{-n}-\omega_{i,j-1/2}^{+n})\mathbf{D}_N]\Delta\mathbf{Q}_{i,j}^{\bar{n}}$$
$$=\Delta t^n\hat{\mathbf{S}}_{i,j}^{n}-\frac{\Delta t^n U_{i,j}^n}{J_{i,j}\Delta\zeta_{i,j}}[\mathscr{H}_{i+1/2,j}^{n}-\mathscr{H}_{i-1/2,j}^{n}]-\frac{\Delta t^n V_{i,j}^n}{J_{i,j}\Delta\eta_{i,j}}[\mathscr{H}_{i,j+1/2}^{n}-\mathscr{H}_{i,j-1/2}^{n}] \tag{50}$$

$$\Theta\omega_{i+1/2,j}^{-n}\mathbf{D}_N\Delta\mathbf{Q}_{i+1,j}^{\hat{n}} - \Theta\omega_{i-1/2,j}^{+n}\mathbf{D}_N\Delta\mathbf{Q}_{i-1,j}^{\hat{n}}$$
$$+\left[\mathbf{I}-\Theta(\omega_{i+1/2,j}^{-n}-\omega_{i-1/2,j}^{+n})\mathbf{D}_N-\Theta\Delta t^n\left(\frac{\partial\hat{\mathbf{S}}}{\partial\mathbf{Q}}\right)_{i,j}^{n}\right]\Delta\mathbf{Q}_{i,j}^{\hat{n}}=\Delta\mathbf{Q}_{i,j}^{\bar{n}} \tag{51}$$

$$\mathbf{Q}_{i,j}^{\hat{n}} = \mathbf{Q}_{i,j}^{n} + \Delta\mathbf{Q}_{i,j}^{\hat{n}} \tag{52}$$

As before, $\Delta\mathbf{W}_{i,j}^{\hat{n}}$ and $\Delta\mathbf{Q}_{i,j}^{\hat{n}}$ denote intermediate solutions and $\hat{\mathscr{F}}_{i+1/2,j}^{n}$, $\hat{\mathscr{G}}_{i,j+1/2}^{n}$, $\mathscr{H}_{i+1/2,j}^{n}$, and $\mathscr{H}_{i,j+1/2}^{n}$ are numerical flux functions. The parameter Θ again controls the temporal discretization of the algorithm. For $\Theta \neq 0$, the partially-decoupled scheme is implicit. The time-differencing is Euler explicit for $\Theta = 0$, trapezoidal implicit for $\Theta = 1/2$, and Euler implicit for $\Theta = 1$.

For the fully implicit algorithm, the numerical flux functions of the gas-dynamic and thermodynamic subsystems are specified as follows. The left-hand-side (LHS) implicit terms of the flux functions are represented in (47)–(52) by the products $\nu^{-}\mathbf{e}\mathbf{A}^{-}$, $\nu^{\mp}\mathbf{e}\mathbf{B}^{\mp}$, $\nu^{+}\mathbf{e}\mathbf{C}^{+}$, and $\omega^{\mp}\mathbf{D}_N$. These are 7×7 and $N_D \times N_D$ influence matrices. In the ζ-direction, the right-hand-side

(RHS) explicit terms of the numerical flux functions are given by:

$$\frac{\Delta t^n}{J_{i,j}\Delta\zeta_{i,j}}[\hat{\mathscr{F}}^n_{i+1/2,j}-\hat{\mathscr{F}}^n_{i-1/2,j}]$$

$$=\sum_{k=1}^{7}[\nu^{-n}_{i+1/2,j,k}\Delta\mathbf{W}^n_{i+1/2,j,k}+\nu^{+n}_{i-1/2,j,k}\Delta\mathbf{W}^n_{i-1/2,j,k}$$

$$+\frac{1-\theta}{4}(\phi^{-n}_{i+1/2,j,k}\nu^{-n}_{i+1/2,j,k}\Delta\mathbf{W}^n_{i+1/2,j,k}-\phi^{-n}_{i+3/2,j,k}\nu^{-n}_{i+3/2,j,k}\Delta\mathbf{W}^n_{i+3/2,j,k})$$

$$+\frac{1+\theta}{4}(\tilde{\phi}^{-n}_{i-1/2,j,k}\nu^{-n}_{i-1/2,j,k}\Delta\mathbf{W}^n_{i-1/2,j,k}-\tilde{\phi}^{-n}_{i+1/2,j,k}\Delta\mathbf{W}^n_{i+1/2,j,k}\nu^{-n}_{i+1/2,j,k})$$

$$+\frac{1+\theta}{4}(\phi^{+n}_{i+1/2,j,k}\nu^{+n}_{i+1/2,j,k}\Delta\mathbf{W}^n_{i+1/2,j,k}-\phi^{+n}_{i-1/2,j,k}\nu^{+n}_{i-1/2,j,k}\Delta\mathbf{W}^n_{i-1/2,j,k})$$

$$+\frac{1-\theta}{4}(\tilde{\phi}^{+n}_{i-1/2,j,k}\nu^{+n}_{i-1/2,j,k}\Delta\mathbf{W}^n_{i-1/2,j,k}-\tilde{\phi}^{+n}_{i-3/2,j,k}\nu^{+n}_{i-3/2,j,k}\Delta\mathbf{W}^n_{i-3/2,j,k})] \quad (53)$$

and

$$\frac{\Delta t^n U^n_{i,j}}{J_{i,j}\Delta\zeta_{i,j}}[\mathscr{H}^n_{i+1/2,j}-\mathscr{H}^n_{i-1/2,j}]$$

$$=\sum_{k=1}^{2N+1}[\omega^{-n}_{i+1/2,j}\Delta\mathbf{H}^n_{i+1/2,j,k}+\omega^{+n}_{i-1/2,j}\Delta\mathbf{H}^n_{i-1/2,j,k}$$

$$+\frac{1-\theta}{4}(\psi^{-n}_{i+1/2,j,k}\omega^{-n}_{i+1/2,j}\Delta\mathbf{H}^n_{i+1/2,j,k}-\psi^{-n}_{i+3/2,j,k}\omega^{-n}_{i+3/2,j}\Delta\mathbf{H}^n_{i+3/2,j,k})$$

$$+\frac{1+\theta}{4}(\tilde{\psi}^{-n}_{i-1/2,j,k}\omega^{-n}_{i-1/2,j}\Delta\mathbf{H}^n_{i-1/2,j,k}-\tilde{\psi}^{-n}_{i+1/2,j,k}\omega^{-n}_{i+1/2,j}\Delta\mathbf{H}^n_{i+1/2,j,k})$$

$$+\frac{1+\theta}{4}(\psi^{+n}_{i+1/2,j,k}\omega^{+n}_{i+1/2,j}\Delta\mathbf{H}^n_{i+1/2,j,k}-\psi^{+n}_{i-1/2,j,k}\omega^{+n}_{i-1/2,j}\Delta\mathbf{H}^n_{i-1/2,j,k})$$

$$+\frac{1-\theta}{4}(\tilde{\psi}^{+n}_{i-1/2,j,k}\omega^{+n}_{i-1/2,j}\Delta\mathbf{H}^n_{i-1/2,j,k}-\tilde{\psi}^{+n}_{i-3/2,j,k}\omega^{+n}_{i-3/2,j}\Delta\mathbf{H}^n_{i-3/2,j,k})] \quad (54)$$

Similar expressions are used to compute the explicit terms of the η-direction flux functions.

In (47)–(54), $\nu^{\pm n}_{i+1/2,j,k}$, $\nu^{\pm n}_{i,j+1/2,k}$, $\omega^{\pm n}_{i+1/2,j}$, and $\omega^{\pm n}_{i,j+1/2}$ are the positive and negative CFL numbers defined by:

$$\nu^{\pm n}_{i+1/2,j,k}=\tfrac{1}{2}(\nu^n_{i+1/2,j,k}\pm|\nu^n_{i+1/2,j,k}|\pm\delta\nu^n_{i+1/2,j,k})$$
$$\nu^{\pm n}_{i,j+1/2,k}=\tfrac{1}{2}(\nu^n_{i,j+1/2,k}\pm|\nu^n_{i,j+1/2,k}|\pm\delta\nu^n_{i,j+1/2,k}) \quad (55)$$

$$\omega^{\pm n}_{i+1/2,j}=\tfrac{1}{2}(\omega^n_{i+1/2,j}\pm|\omega^n_{i+1/2,j}|\pm\delta\omega^n_{i+1/2,j})$$
$$\omega^{\pm n}_{i,j+1/2}=\tfrac{1}{2}(\omega^n_{i,j+1/2}\pm|\omega^n_{i,j+1/2}|\pm\delta\omega^n_{i,j+1/2}) \quad (56)$$

for which $\delta\nu$ and $\delta\omega$ are wave speed corrections that ensure that solutions are physically realistic. The seven-component column vectors $\mathbf{A}^{-n}_{i+1/2,j,k}$, $\mathbf{B}^{\mp n}_{i\pm1/2,j,k}$, and $\mathbf{C}^{+n}_{i-1/2,j,k}$ are defined by:

$$\mathbf{A}^{-n}_{i+1/2,j,k}=\frac{\partial\alpha^n_{i+1/2,j,k}}{\partial\mathbf{W}^n_{i+1,j}},\qquad \mathbf{B}^{\mp n}_{i\pm1/2,j,k}=\frac{\partial\alpha^n_{i\pm1/2,j,k}}{\partial\mathbf{W}^n_{i,j}},\qquad \mathbf{C}^{+n}_{i-1/2,j,k}=\frac{\partial\alpha^n_{i-1/2,j,k}}{\partial\mathbf{W}^n_{i-1,j}} \quad (57)$$

where $\alpha^n_{i\pm 1/2,j,k}$ are again given by (28)–(31). The column vectors $\mathbf{A}^{-n}_{i,j+1/2,k}$, $\mathbf{B}^{\mp n}_{i,j\pm 1/2,k}$, and $\mathbf{C}^{+n}_{i,j-1/2,k}$ are similarly defined. The quantity $\mathbf{D}_N$ is a $N_D \times N_D$ diagonal matrix with diagonal elements $(\delta_{11}, \delta_{22}, \ldots, \delta_{N_D-1 N_D-1}, 0)$. Finally, the terms $v^n_{i+1/2,j,k}$, $v^n_{i,j+1/2,k}$ $\Delta\mathbf{W}^n_{i+1/2,j,k}$, $\Delta\mathbf{W}^n_{i,j+1/2,k}$, $\alpha^n_{i+1/2,j,k}$, $\alpha^n_{i,j+1/2,k}$, $\mathbf{e}^n_{i+1/2,j,k}$, $\mathbf{e}^n_{i,j+1/2,k}$, $\omega^n_{i+1/2,j}$, $\omega^n_{i,j+1/2}$, $\Delta\mathbf{H}^n_{i+1/2,j,k}$, $\Delta\mathbf{H}^n_{i,j+1/2,k}$, $\mathbf{N}_{W_k}$, $\mathbf{N}_{H_k}$, $\partial\hat{\mathbf{S}}/\partial\mathbf{Q}$, Θ, $\mathbf{I}$, and N_D are as defined for the semi-implicit scheme of the previous subsection.

The unlimited schemes of Osher and Chakravarthy are combinations of second-order central and fully upwind differences. In (53) and (54), θ controls the spatial discretization. Values of $\theta = 1/3$, -1, 0, 1/2, and 1 result in the third-order, fully-upwind, Fromm's method, low-truncation-error second-order, and central differencing schemes, respectively. A value of $\theta = -1/3$ provides a fifth second-order scheme which does not appear to have a name. The truncation error of the semi-discrete schemes decreases in the order $\theta = -1$, 1, $-1/3$, 0, 1/3, and 1/2. The use of the central-difference or fully-upwind formulations is not recommended. This is because the unlimited semi-discrete central-difference scheme ($\theta = 1$) is non-dissipative and therefore unreliable, and the fully-upwind scheme ($\theta = -1$) has the greatest truncation error. Chakravarthy and Osher[14] note that Fromm's formulation ($\theta = 0$) provides the highest accuracy in nozzle flow calculations with sonic points.

Like Roe's method, the high-order upwind schemes of Chakravarthy and Osher attain their TVD properties by employing flux limiters. The flux limiters $\phi^{\pm n}_{i+1/2,j,k}$ and $\tilde{\phi}^{\pm n}_{i+1/2,j,k}$ are specified by:

$$\phi^{\pm n}_{i+1/2,j,k} = \varphi(b^{\pm n}_{i+1/2,j,k}), \qquad \tilde{\phi}^{\pm n}_{i+1/2,j,k} = \varphi(\tilde{b}^{\pm n}_{i+1/2,j,k}) \tag{58}$$

where the flux limiter function $\varphi(b) = \max(0, \min(1, \beta b))$ is used, $b^{\pm n}_{i+1/2,j,k}$ and $\tilde{b}^{\pm n}_{i+1/2,j,k}$ are flux ratios given by:

$$b^{\pm n}_{i+1/2,j,k} = \frac{v^{\pm n}_{i-1/2,j,k}(\Delta\mathbf{W}^n_{i-1/2,j,k}\cdot\mathbf{N}_{W_k})}{v^{\pm n}_{i+1/2,j,k}(\Delta\mathbf{W}^n_{i+1/2,j,k}\cdot\mathbf{N}_{W_k})}, \qquad \tilde{b}^{\pm n}_{i+1/2,j,k} = \frac{v^{\pm n}_{i+3/2,j,k}(\Delta\mathbf{W}^n_{i+3/2,j,k}\cdot\mathbf{N}_{W_k})}{v^{\pm n}_{i+1/2,j,k}(\Delta\mathbf{W}^n_{i+1/2,j,k}\cdot\mathbf{N}_{W_k})} \tag{59}$$

and β is a compression parameter chosen in the interval $0 \leqslant \beta \leqslant (3-\theta)/(1-\theta)$. If $\beta \geqslant 1$, higher-order spatial accuracy is obtained. Larger values of β result in greater compression of discontinuities. Comparable expressions are used for evaluating the other flux limiters $\phi^{\pm n}_{i,j+1/2,k}$, $\tilde{\phi}^{\pm n}_{i,j+1/2,k}$, $\psi^{\pm n}_{i+1/2,j}$, $\tilde{\psi}^{\pm n}_{i+1/2,j}$, $\psi^{\pm n}_{i,j+1/2}$, and $\tilde{\psi}^{\pm n}_{i,j+1/2}$.

In the current work, the wave speed corrections δv and $\delta\omega$ are determined from a modified form of the entropy correction of Harten[5] as suggested by Yee *et al.*[58]. The wave speed correction $\delta v^n_{i+1/2,j,k}$ is specified by:

$$\delta v^n_{i+1/2,j,k} = \frac{\Delta t^n}{J_{i+1/2,j}\Delta\zeta_{i+1/2,j}}\left[\frac{(\lambda^n_{i+1/2,j,k})^2 + \varepsilon^2}{2\varepsilon} - |\lambda^n_{i+1/2,j,k}|\right] \tag{60}$$

where ε is a small positive number, with a larger value enhancing the entropy enforcement at the expense of solution accuracy. Yee *et al.* have found that a variable or solution dependent ε is required for hypersonic blunt-body flows. They suggest ε have the form:

$$\varepsilon = \tilde{\varepsilon}\left[|U| + |V| + \frac{a}{2}\left(\sqrt{x_\eta^2 + y_\eta^2} + \sqrt{x_\zeta^2 + y_\zeta^2}\right)\right] \tag{61}$$

where $\tilde{\varepsilon}$ is a constant ($0.05 < \tilde{\varepsilon} \leqslant 0.25$) and U, V, and a are the appropriate Roe-average values. Equivalent formulations are used to specify $\delta v^n_{i,j+1/2,k}$, $\delta\omega^n_{i+1/2,j,k}$, and $\delta\omega^n_{i,j+1/2,k}$. Note that the inclusion of the wave speed corrections in the evaluation of the higher-order antidiffusive fluxes results in a consistent high-resolution scheme.

Linear stability theory indicates that the solution algorithm of (46)–(52) is unconditionally stable for $\Theta = 1$. However, this result is somewhat misleading because TVD schemes are very often non-linearly stable even though the underlying unlimited non-TVD version is shown to be linearly unstable[57]. Moreover, in practice, the time step Δt^n is restricted by linearization and factorization errors. In this study, it was found that optimum CFL numbers C_{CFL} as defined by

(45) for steady-state convergence are in the range $1 < C_{CFL} < 10$, although even smaller time steps may be required in cases where the source terms are extremely stiff.

Equations (47), (48), (50), and (51) represent block and scalar tridiagonal systems of linear equations which must be solved for the solution changes. A close inspection of these equations reveals that, for a given iteration level, the factored implicit solution of the gas-dynamic subsystem only requires the solution of 7×7 block tridiagonal systems of linear equations in each sweep direction. Moreover, the thermodynamic subsystem does not require the solution of full block tridiagonal systems in either sweep direction. In the η-direction, $2N$ scalar tridiagonal systems must be solved for each sweep and, in the ζ-direction, the submatrices of the off-diagonal blocks forming the $N_D \times N_D$ block tridiagonal systems contain only diagonal elements. Although not carried out here, block tridiagonal matrix inversion routines can be devised to account for the simplified structure of these off-diagonal submatrices and, thereby, reduce the computational effort required for each ζ-sweep. For large thermodynamic systems (i.e., $N > 5$), additional computational savings may be realized if, as suggested by Bussing and Murman[34], the source Jacobian matrices $\partial\hat{\mathbf{S}}/\partial\mathbf{Q}$ are diagonalized by neglecting the off-diagonal influence coefficients. This would simplify the system of linear equations representing each ζ-sweep and it would then only be necessary to solve N_D scalar tridiagonal systems in both sweep directions. All of this make the proposed partially-decoupled fully implicit scheme potentially more attractive than fully coupled factored implicit schemes, which require the solution of $(2N + 4) \times (2N + 4)$ block tridiagonal systems in both sweep directions.

It has been suggested by Yee and Shinn[33] that approximate factorization and/or alternating-direction-implicit (ADI) procedures may not be appropriate for the solution of non-equilibrium flows because the stiff source terms can make the factored or ADI algorithm inefficient. However, this observation concerned fully coupled solution algorithms. The gas-dynamic subsystem of the present partially-decoupled approach contains only homogeneous terms. The stiff source terms are only present in the thermodynamic subsystem. Furthermore, Molvik and Merkle[38] have successfully applied a factored implicit scheme to predict non-equilibrium flows and Shih and Chyu[59] discuss various approximate factorization methodologies for systems of equations with source terms and suggest techniques for reducing the factorization errors when the source terms are large. In the present study, it was found that by choosing the time step so as to maintain the diagonal dominance of the implicit operators of the thermodynamic subsystem and performing subiterations on the thermodynamic subsystem without updating the gas-dynamic subsystem as needed (the capability of performing subiterations on either subsystem for steady or unsteady problems is another computation-saving feature permitted by the partially-decoupled approach), steady-state solutions were obtained within a reasonable number of iterations. Further research is required to examine whether the convergence of the factored implicit algorithm can be significantly improved by employing convergence enhancing methods such as local time stepping, diagonalization, and/or multigrid procedures, or whether unfactored implicit schemes, such as point and line relaxation techniques (e.g., refer to References 33, 35–37, and 57), provide steady-state solutions in a more efficient manner.

Boundary conditions

Boundary conditions are required for prescribing the numerical solution at the extremities of the computational domain. For the example problems considered here, two types of approximate boundary conditions are required: a transmissive or nonreflecting far-field outflow boundary condition and a reflection or solid-wall boundary condition.

Reflection boundary conditions at solid boundaries are applied by enforcing flow tangency and employing the frozen-flow Rankine–Hugoniot and Riemann invariant relations across unsteady surface-normal shocks and rarefaction waves to determine the various solution properties. Non-reflecting boundary conditions are implemented by employing a constant

extrapolation technique[60]. If the flux limiters at the boundary node are set to zero, thereby reducing the differencing to first order, this form of boundary condition is known to permit out-going waves, propagating normal to the boundary, to leave the domain without the formation of unwanted numerical disturbances. Although more sophisticated non-reflecting boundary conditions can be applied by using a characteristic extrapolation technique[60], the simplified lower-order approach is sufficient for the present calculations. Note that for general flows, constant extrapolation should be employed with caution. The method is appropriate for supersonic outflows in which disturbances cannot travel upstream. However, the boundary condition is over-determined and invariably incorrect for subsonic outflow and subsonic and supersonic inflows. This is because the solution state at the boundary is prescribed entirely by the interior solution and does not necessarily correctly represent the physics of the flow outside the computational domain.

THERMODYNAMIC MODEL FOR AIR

A number of numerical examples are presented in the next section to verify the proposed semi-implicit and fully implicit TVD methods and demonstrate the capabilities of the algorithms for predicting non-equilibrium vibrationally relaxing and chemically reacting flows. The test flows include non-equilibrium flows of air as well as pure oxygen and nitrogen. A five-species (N_2, O_2, NO, N, and O) four-temperature (i.e., translational–rotational temperature T, and vibrational energies e_{vN_2}, e_{vN_2}, and e_{vNO}) non-equilibrium thermodynamic model for air is used in all of the computations. This model is valid for temperatures up to 8000 K and pressures above about 0.1 kPa and can be used to represent the flows of pure oxygen and nitrogen by setting the mass concentrations of the other species to zero. For temperatures above 8000 K, ionization and other rate processes become significant.

The dissociation-recombination reaction mechanism of air is represented in the model by following the elementary reactions:

$$\begin{aligned} O_2 + M &\rightleftharpoons 2O + M \\ N_2 + M &\rightleftharpoons 2N + M \\ NO + M &\rightleftharpoons N + O + M \\ NO + O &\rightleftharpoons N + O_2 \\ N_2 + O &\rightleftharpoons NO + N \end{aligned} \tag{62}$$

where M is a collision partner or *catalytic molecule*; it can be any one of the five species. Seventeen elementary reactions (fifteen dissociation/recombination and two exchange reactions) are represented by the reaction scheme of (62). The forward reactions of the first three reaction equations above are *bimolecular* dissociation reactions (reactions involving the collision of two molecules) and the associated reverse reactions are *termolecular* recombination reactions (reactions involving the collision of three molecules). The forward and reverse reactions of the fourth and fifth reaction equations are bimolecular exchange or shuffle reactions involving NO. The forward exchange reactions are fast compared with the dissociation reactions and are important in establishing the concentrations of NO and N in many flow situations.

Collision theory and the law of mass action are used to describe the finite-rate reaction processes from which empirical expressions for the net time rate of change of the species concentrations may be obtained. The expressions take the form[42,43]

$$w_s = \frac{\mathcal{M}_s}{\rho} \sum_{r=1}^{N_R} (\sigma_{s,r}^b - \sigma_{s,r}^f) \left\{ k_r^f \prod_{s'=1}^{N} \left(\frac{c_{s'}\rho}{\mathcal{M}_{s'}} \right)^{\sigma_{s',r}^f} - k_r^b \sum_{s'=1}^{N} \left(\frac{c_{s'}\rho}{\mathcal{M}_{s'}} \right)^{\sigma_{s',r}^b} \right\} \tag{63}$$

where $\sigma^f_{s,r}$ and $\sigma^b_{s,r}$ are the stoichiometric coefficients of the reactant and product species s of the reaction r, k^f_r and k^b_r are the forward and backward reaction rates of reaction r, and $\mathcal{M}_s$ is the molecular weight of species s. The variable N_R represents the total number of elementary reactions (in this case, $N_R = 17$). The reaction rates are assumed to be functions of the translational–rotational temperature and are described by modified forms of the Arrhenius equation. They can be written as:

$$k^f_r = C^f_r T^{n^f_r} \exp\left(\frac{-E^f_r}{KT}\right), \qquad k^b_r = C^b_r T^{n^f_r} \exp\left(\frac{-E^b_r}{KT}\right) \tag{64}$$

where K is Boltzmann's constant. The reaction rate coefficients C^f_r, C^b_r, n^f_r, n^b_r, E^f_r, and E^b_r are taken from the data set compiled by Dunn and Kang[61].

The finite-rate vibrational relaxation of the diatomic molecules N_2, O_2, and NO is represented in the model by assuming that vibrationally excited molecules behave as ideal harmonic oscillators. It is further assumed that the relaxation process from an excited non-equilibrium state to a state of thermodynamic equilibrium occurs only through translational–vibrational collisions. It then follows that the time rate of change of the vibrational energy e_{v_s} of the species s may be prescribed by the so-called Landau–Teller law having the form[42,43]:

$$q_s = \frac{e^*_{v_s} - e_{v_s}}{\tau_s} \tag{65}$$

where $e^*_{v_s}$ is the equilibrium vibrational energy given by:

$$e^*_{v_s} = \frac{\Theta_{v_s} R_s}{\exp(\Theta_{v_s}/T) - 1} \tag{66}$$

and τ_s is the characteristic relaxation time. The characteristic vibrational temperatures Θ_{vN_2}, Θ_{vO_2}, and Θ_{vNO} are taken to be 3353, 2239, and 2699 K, respectively. The semi-empirical correlations of Millikan and White[62]:

$$\tau_s = \frac{\sum_{s'} \frac{c_{s'}}{\mathcal{M}_{s'}} \exp\left[\mathcal{A}_s\left(T^{-1/3} - 0.015\left(\frac{\mathcal{M}_s \mathcal{M}_{s'}}{\mathcal{M}_s + \mathcal{M}_{s'}}\right)^{1/4}\right) - 18.42\right]}{p \sum_{s'} \frac{c_{s'}}{\mathcal{M}_{s'}}} \tag{67}$$

based on modifications to the Landau–Teller equation are used to determine τ_s, where $\mathcal{A}_{N_2}$, $\mathcal{A}_{O_2}$, and $\mathcal{A}_{NO}$ are assumed to have values of 220, 129, and 168, respectively, and the units of pressure, temperature, and molecular weight are atmospheres, Kelvin, and grams per mole.

It should be noted that the preceding chemical and vibrational rate equations have been derived from theoretical considerations and analyses which do not encompass the coupling that is known to exist between the chemical reaction and vibrational relaxation processes. Chemical-vibrational coupling (CVC) effects can be important, and both preferential CVC models ($\beta_s > 1$) and non-preferential CVC models ($\beta_s = 1$) have been proposed[44]. However, these effects are not included here and a value of unity is used for β_s in all of the computations which now follow.

NUMERICAL RESULTS AND DISCUSSION

The validity of the partially-decoupled semi-implicit and fully implicit TVD algorithms is now illustrated by investigating five different test flows. The flow problems considered are as follows: the single, complex, and double Mach reflections of a planar incident shock from a wedge in air; the diffraction of a planar high-Mach-number incident shock at an expansion corner in

oxygen; and the hypersonic flow of nitrogen over a cylindrical blunt body. All of the flows possess complicated shock structure and in most cases exhibit substantial vibrational and chemical non-equilibrium effects. They have also been investigated experimentally, thus making them worthy test problems. Of these flows, the three oblique shock-wave reflections and one shock-wave diffraction are non-stationary flow problems and the blunt-body flow is a stationary flow problem. The unsteady cases are considered for the purposes of validating the semi-implicit solver and the steady case is used to validate the fully implicit scheme. The five-species four-temperature thermodynamic model described in the previous section is used in all of the computations.

Single Mach reflection in air

In this and the following two subsections, numerical predictions of the semi-implicit TVD scheme are presented for three different types of non-stationary oblique shock-wave reflections in air and compared directly to experimental data. Deschambault and Glass[63,64] have conducted an extensive experimental investigation of regular and Mach reflections in air at the University of Toronto Institute for Aerospace Studies (UTIAS). The experiments were performed in the UTIAS 10 cm by 18 cm hypervelocity shock tube and a Mach–Zehnder interferometer was used to obtain infinite fringe interferograms of the flow-fields. These experiments are an excellent source of benchmark data for the validation of computer codes and numerical algorithms developed for solving unsteady compressible flow problems with complex non-linear wave interactions. A number of recent studies have made direct comparisons between the interferometric results and numerical predictions of other sophisticated shock-capturing schemes. See, for example, References 17, 29, and 65. For the experiments in which dissociation and vibrational relaxation effects are negligible, the interferograms provide direct observations of the flow isopycnics (lines of constant density). For the higher shock-Mach-number cases in which non-equilibrium effects are significant, the fringe patterns of the interferograms provide qualitative information about the flow-field density distribution and shock structure.

The first shock reflection problem considered is the oblique reflection of a $M_s = 2.03$ planar shock wave propagating in air incident on a 27° compression corner. A schematic diagram of the resulting single Mach reflection pattern is given in *Figure 1*. The incident and reflected

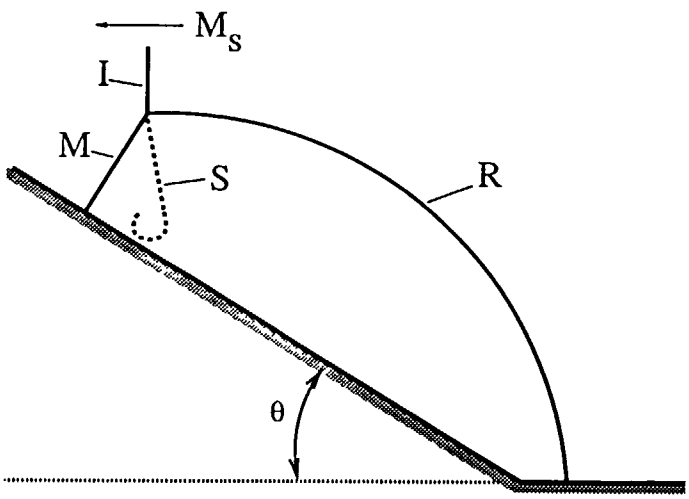

Figure 1 Schematic diagram of single Mach reflection; I, incident shock; R, reflected shock; M, Mach stem; S, slipstream

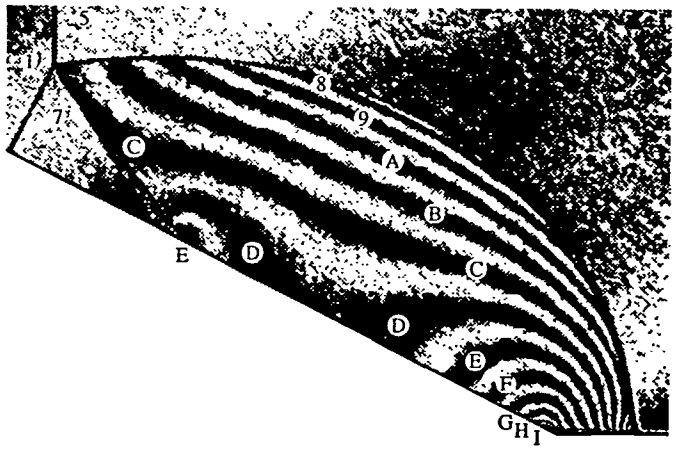

ρ/ρ_0					
	1 1.00	5 2.73	9 3.49	D 3.80	H 4.12
	2 1.50	6 3.00	A 3.57	E 3.88	I 4.20
	3 2.00	7 3.40	B 3.65	F 3.96	
	4 2.50	8 3.41	C 3.73	G 4.04	

Figure 2 Single Mach reflection; $M_s = 2.03$, $\theta = 27°$, $p_0 = 33.25$ kPa, $T_0 = 299.2$ K. Interferogram and experimentally determined isopycnics

shocks, along with the Mach stem and slipstream, are shown. The pressure p_0 and temperature T_0 of the quiescent air ahead of the shock are 33.25 kPa and 299.2 K, respectively. The density ρ_0 is 0.387 kg/m^3. The equilibrium flow Mach number and temperature behind the incident shock are about 0.99 and 507 K, respectively. Although non-equilibrium effects are insignificant for this first problem, it provides an excellent test of the capabilities of the gas-dynamic solver for predicting complicated shock structure. The experimental interferogram obtained by Deschambault and Glass is shown in *Figure 2*. In this case, the temperatures are low and each fringe of the interferogram corresponds to an actual isopycnic. The density difference $\Delta\rho$ between any two fringes can be related by:

$$\Delta\rho = \frac{\lambda}{\mathscr{K} l} \tag{68}$$

where λ is the wavelength of the interferometer light source, $\mathscr{K}$ is the Gladstone–Dale constant of the gas, and l is the depth of the test section. The corresponding isopycnics as determined from an analysis of the interferometric fringe pattern using (68) (refer to Reference 63 for details) are also given in *Figure 2*.

The predicted density contours of the single Mach reflection flow field are depicted in *Figure 3*. The labelled density contours shown in this Figure are nearly identical to the isopycnics shown in *Figure 2*. A 312 × 104 node mesh was used in the numerical computation, van Leer's flux limiter was used for the nonlinear characteristic fields (i.e., $k = 1$ and 7 for the gas-dynamic subsystem), and the superbee limiter was employed for the linearly degenerate fields. As is the case for all of the shock reflection and diffraction problems considered herein, the initial data for the computations were specified by locating the incident shock upstream of the corner and using the Rankine–Hugoniot conditions to prescribe the equilibrium post-shock state.

By comparing *Figures 2* and *3*, it is readily apparent that the proposed partially-decomposed semi-implicit TVD scheme accurately reproduces the general structure of the flow field. The

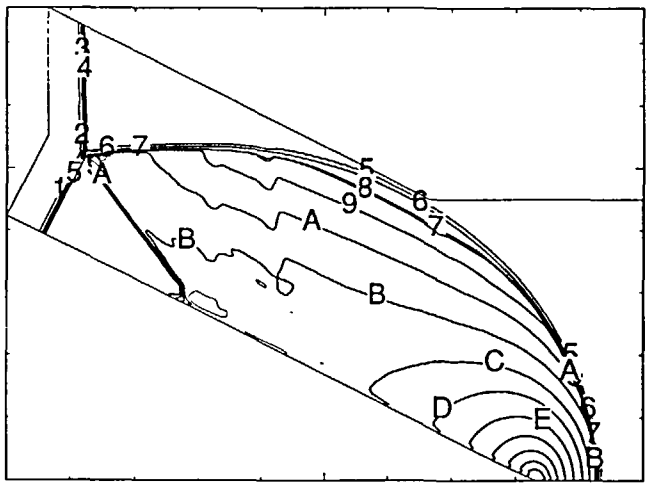

Figure 3 Single Mach reflection; $M_s = 2.03, \theta = 27°, p_0 = 33.25$ kPa, $T_0 = 299.2$ K. Predicted constant density contours

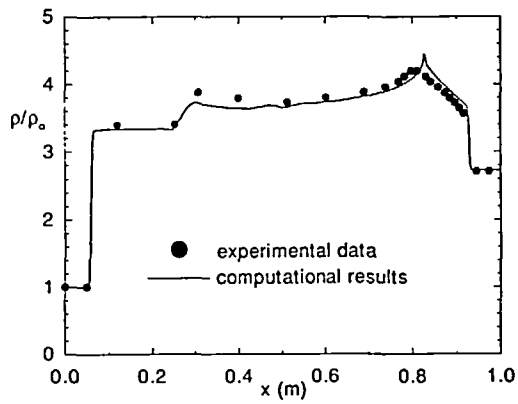

Figure 4 Single Mach reflection; $M_s = 2.03$, $\theta = 27°$, $p_0 = 33.25$ kPa, $T_0 = 299.2$ K. Predicted and measured wall density distributions

predicted reflected shock is detached from the corner of the wedge, as in the experiment, and its shape is very similar to that of the reflected shock in the interferogram. The position of the triple point appears to be well predicted, as is the slipstream position. Furthermore, the qualitative and quantitative agreement between the two sets of isopycnics is very good. This is true even in the reflected flow region, which can be difficult to predict accurately. These findings are further supported by the additional comparisons of the predicted and measured distributions of the density along the wall of the compression corner shown in *Figure 4* (the experimental values are interpreted from the interferogram). Overall, it can be said that the agreement between calculation and experiment is very good.

Complex Mach reflection in air

The next test flow problem considered is the non-stationary oblique reflection of a $M_s = 10.37$ planar shock wave propagating in air incident on a 10° compression corner. Again the calculations

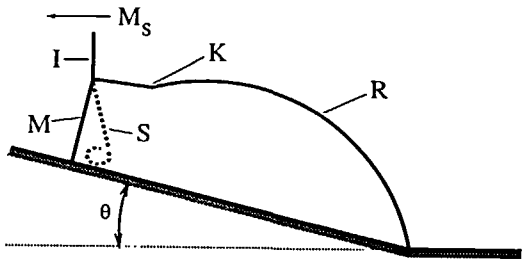

Figure 5 Schematic diagram of complex Mach reflection; I, incident shock; R, reflected shock, M. Mach stem; S, slipstream; K, kink

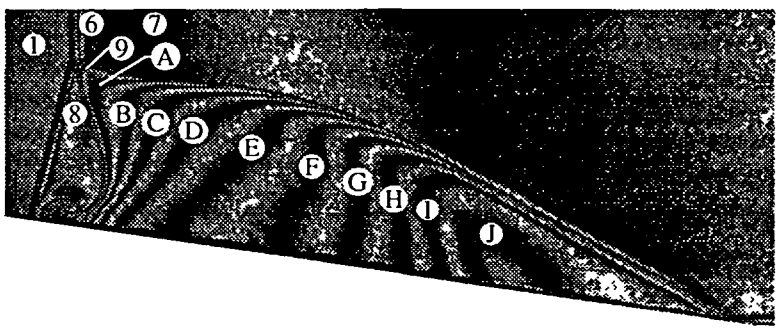

ρ/ρ_0					
	1 1.00	5 8.73	9 10.64	D 12.19	H 13.74
	2 2.00	6 8.72	A 11.03	E 12.58	I 14.12
	3 4.00	7 9.11	B 11.42	F 12.96	J 14.51
	4 6.00	8 9.67	C 11.80	G 13.35	

Figure 6 Complex Mach reflection; $M_s = 10.37$, $\theta = 10°$, $p_p = 6.67$ kPa, $T_0 = 299$ K. Interferogram and experimentally determined isopycnics

are compared to the experimental data of Deschambault and Glass. A schematic diagram of the resulting complex Mach reflection pattern is given in *Figure 5*. The incident and reflected shocks along with the Mach stem, slipstream, and kink are all shown. The pressure p_0, density ρ_0, and temperature T_0 ahead of the shock are 6.67 kPa, 0.0777 kg/m^3, and 299 K, respectively. Under these conditions, the state of the air behind the incident shock exhibits substantial high temperature effects. The post-shock equilibrium state temperature is about 4,040 K, the flow Mach number is 2.6, and the degree of dissociation of the diatomic molecules is about 10% ($c_{N_2} = 0.731$, $c_{O_2} = 0.098$, $c_{NO} = 0.077$, $c_N < 0.001$, and $c_O = 0.094$). Furthermore, the chemical and vibrational relaxation lengths behind the incident shock are of the order of 1–5 mm, which is quite large when compared to the characteristic dimensions of experimental flow field[64], and Glaz *et al.*[29] have demonstrated that a finite-rate non-equilibrium model is required to accurately predict this type of flow.

The experimental interferogram and associated isopycnics for the complex Mach reflection are depicted in *Figure 6*. Note that the values of the isopycnics indicated in *Figure 6* are different from those of Reference 63. The experimental isopycnics have been re-evaluated by first assuming that the state of the air some distance behind the incident shock is equal to the equilibrium state obtained by solving the Rankine–Hugoniot conditions, and then by matching one of the experimental fringes within the reflected shock region to an isopycnic of the semi-implicit TVD

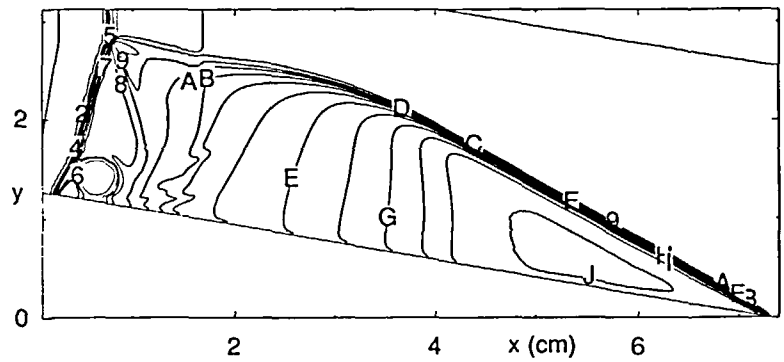

Figure 7 Complex Mach reflection; $M_s = 10.37$, $\theta = 10°$, $p_0 = 6.67$ kPa, $T_0 = 299$ K. Predicted constant density contours

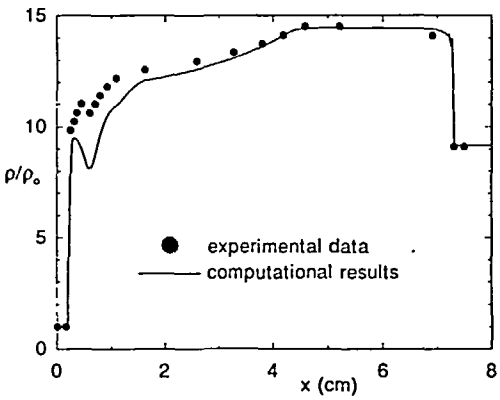

Figure 8 Complex Mach reflection; $M_s = 10.37, \theta = 10°$, $p_0 = 6.67$ kPa, $T_0 = 299$ K. Predicted and measured wall density distributions

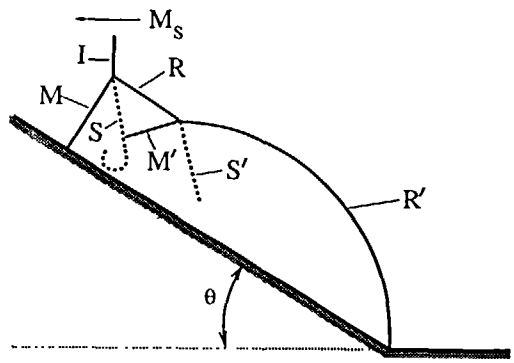

Figure 9 Schematic diagram of double Mach reflection; I, incident shock; R, R′, reflected shocks; M, M′, Mach stems; S, S′, slipstreams

solution. Although it is recognized that the occurrence of dissociation means that the fringes no longer correspond directly to lines of equi-density, as was the case in the previous non-reacting Mach reflection problem, the evaluation procedure for the experimental isopycnics still provides some quantitative information about the flow density distribution.

The predicted density contours of the partially-decoupled semi-implicit scheme for the complex Mach reflection flow field using a 450 × 125 node computational mesh are shown in *Figure 7*. A combination of the minmod and superbee limiters was used. As for the single Mach reflection problem, the overall agreement between the numerical and experimental results of *Figures 6* and *7* can be seen to be quite good. The predicted reflected shock and Mach stem are well resolved and the computed slipstream position and associated vortex roll-up also compare favourably with the experiment. The numerical simulation predicts that the reflected shock is attached and has a distinct kink just behind the incident shock. These features are also observable in the experimental interferogram. In addition, the computed isopycnics appear to agree both qualitatively and quantitatively with experiment. Similar agreement can be observed in the wall density plots of *Figure 8*.

The exaggerated deformation or toe-out of the base of the Mach stem in the numerical computations is the only major difference between the experimental and simulated flow fields.

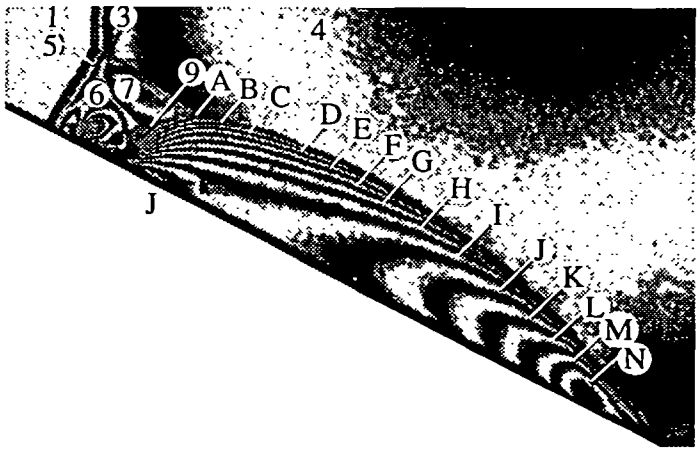

ρ/ρ_0										
	1	1.00	6	10.63	B	15.04	G	18.19	L	21.34
	2	5.00	7	12.52	C	15.67	H	18.82	M	21.97
	3	6.82	8	13.15	D	16.30	I	19.45	N	22.60
	4	8.08	9	13.78	E	16.93	J	20.08		
	5	10.00	A	14.41	F	17.56	K	20.71		

Figure 10 Double Mach reflection; $M_s = 8.7, \theta = 27°, p_0 = 4.097$ kPa, $T_0 = 299.2$ K. Interferogram and experimentally determined isopycnics

The deformation is produced by the interaction of the Mach stem and slipstream vortex. Although some curvature of the Mach stem exists in the actual flow, the interaction process is overpredicted in the numerical simulation, and hence the toe-out of the Mach stem is also overpredicted. This discrepancy is attributed to: (1) the absence of viscous effects in the numerical predictions; and (2) the under-resolution of the complicated solution (i.e., insufficient grid refinement) in the Mach stem region. It is conjectured that further refinement of the discretized solution domain and inclusion of viscous effects would improve the predictions. It is informative to note that the quality of the semi-implicit scheme solutions in the Mach stem region was found to be very dependent on four factors: (1) the type of flux limiting used; (2) orthogonality of the grid with respect to the wall; (3) size of the time step; and (4) uniformity of the grid spacing. By employing almost uniform grids that are orthogonal to the wall and by taking the largest time steps permitted by the CFL criterion, numerical diffusion errors are reduced and higher quality solutions are obtained in this region. Some solution tuning is also possible through the choice of flux limiters.

Double Mach reflection in air

The third test case considered is also a non-stationary oblique reflection problem in which a $M_s = 8.7$ planar shock wave propagating in air is incident on a 27° compression corner and results in a double Mach reflection pattern. A schematic diagram of this flow field is depicted in *Figure 9*. Primary and secondary reflected shocks, Mach stems, and slipstreams are shown. The pressure, density, and temperature ahead of the shock are 4.097 kPa, 0.0477 kg/m^3 and 299.2 K, respectively. Non-equilibrium effects are prevalent in this flow. The equilibrium flow Mach number behind the incident shock is 2.44 and the equilibrium temperature is approximately 3320 K. The equilibrium post-shock state is about 5–6% dissociated with $c_{N_2} = 0.739, c_{O_2} = 0.166$, $c_{N_2} = 0.059$, $c_N < 0.001$, and $c_O = 0.035$. Furthermore, one-dimensional numerical experiments suggest that the non-equilibrium relaxation lengths behind the incident shock are about 3–6 mm.

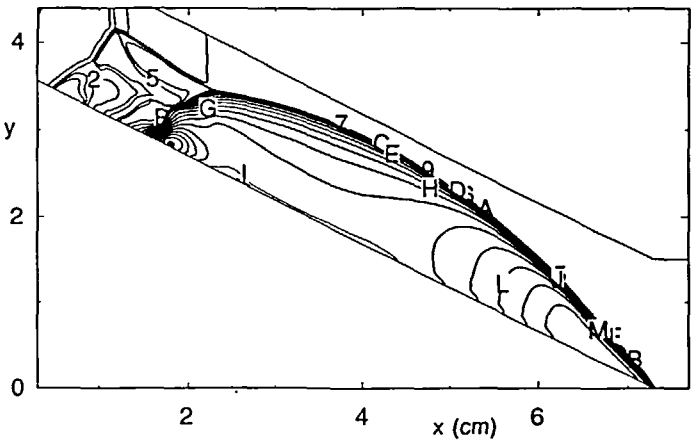

Figure 11 Double Mach reflection; $M_s = 8.7$, $\theta = 27°$, $p_0 = 4.097$ kPa, $T_0 = 299.2$ K. Predicted constant density contours

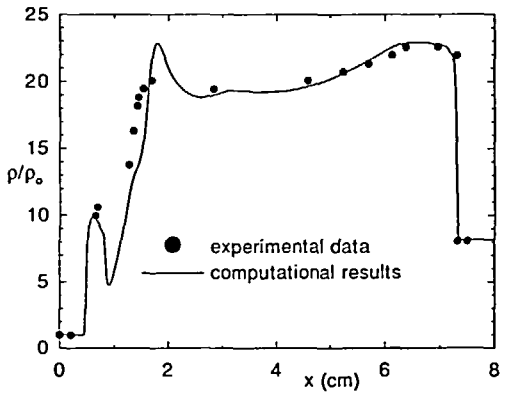

Figure 12 Double Mach reflection; $M_s = 8.7$, $\theta = 27°$, $p_0 = 4.097$ kPa, $T_0 = 299.2$ K. Predicted and measured wall density distributions

The infinite-fringe interferogram of the $M_s = 8.7$ double Mach reflection recorded by Deschambault and Glass is illustrated in *Figure 10*. As with the complex Mach reflection, the approximate values of the experimental isopycnics indicated in the Figure have been re-evaluated using the procedure described in the previous subsection. Shown in *Figure 11* are the predicted contours of constant density for this reflection process obtained by employing the partially-decoupled semi-implicit TVD scheme. The computations were performed using a 486 × 80 node mesh with the minmod flux limiter applied to all characteristic fields. The corresponding experimental and calculated wall density profiles are given in *Figure 12*. It can be seen from *Figures 10–12* that the proposed semi-implicit TVD scheme is capable of reproducing both primary and secondary reflected shocks, Mach stems, and slipstreams. Furthermore, the relaxation region directly behind the incident shock appears to be quite well predicted. Although the toe-out of the Mach stem in the numerical flow field is evident, the agreement between numerical and experimental results is again reasonably good.

It is worth mentioning that the time scales associated with the finite-rate source terms for

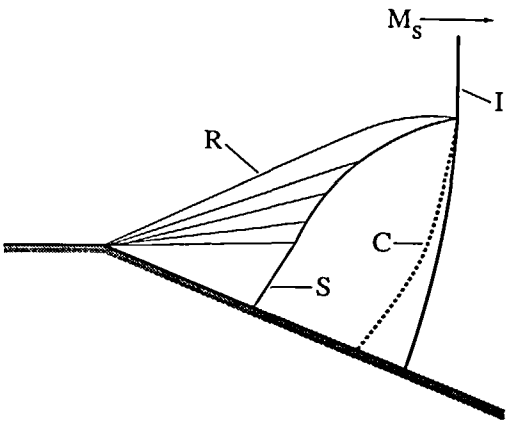

Figure 13 Schematic diagram of shock-wave diffraction at an expansion corner; I, incident shock; R, rarefaction fan; S, recompression shock; C, contact surface

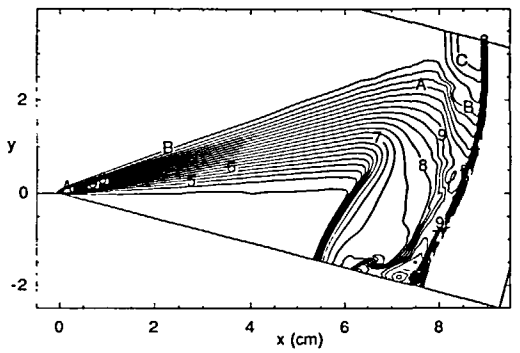

ρ/ρ_0 1 1.00 4 4.67 7 7.67 9 9.67 B 11.67
2 2.67 5 5.67 8 8.67 A 10.67 C 12.67
3 3.67 6 6.67

Figure 14 Shock-wave diffraction; $M_s = 12$, $\theta = 15°$, $p_0 = 2.67$ kPa, $T_0 = 300$ K. Predicted constant density contours

both the complex and double Mach reflection computations were approximately 100–1000 times smaller than the gas-dynamic time scales. The semi-implicit solver effectively removed the stability constraints imposed by the finite-rate time scales and permitted the computations to be performed with the numerical time steps controlled only by the gas-dynamic time scales.

Shock-wave diffraction in oxygen

Another application of the semi-implicit TVD algorithm relates to the prediction of the non-stationary planar flow of dissociated oxygen around a 15° expansion corner. This flow is generated by the diffraction of a $M_s = 12$ planar shock wave. The pressure p_0, density ρ_0, and temperature T_0 of the quiescent oxygen ahead of the shock are 2.67 kPa, 0.0342 kg/m^3, and 300 K, respectively. The frozen flow Mach number behind the shock is 2.7 and the temperature is about 3825 K. The post-shock state of the oxygen is approximately 23% dissociated. The classical shock-wave diffraction pattern is shown in the diagram of *Figure 13*. The Figure illustrates the Prandtl–Meyer expansion wave and the recompression shock and associated contact surface. A strong non-equilibrium recombination process occurs through the rarefaction wave fan after the high-Mach-number shock passes the corner.

The shock diffraction problem was computed using the semi-implicit algorithm and a 308 × 156 node grid. A combination of the van Leer and superbee flux limiters was used. The predicted density contours at a time 26.5 μs after the shock has passed the corner are given in *Figure 14*. The recompression shock and contact surface are clearly evident in the Figure and appear to be well resolved. The fan of the stationary rarefaction wave evolving from the corner can also be observed.

An experimental study of the flow of dissociated oxygen around expansion corners was carried out by Drewry[66,67] in the UTIAS 10 cm by 18 cm hypervelocity shock tube. Comparisons of the predicted isopycnics of *Figure 14* to schlieren photographs (Fig. 33a and Fig. 35 of Reference 66) reveal that the general features of the flow field are duplicated by the present numerical method, including the shapes and relative positions of the recompression shock and contact

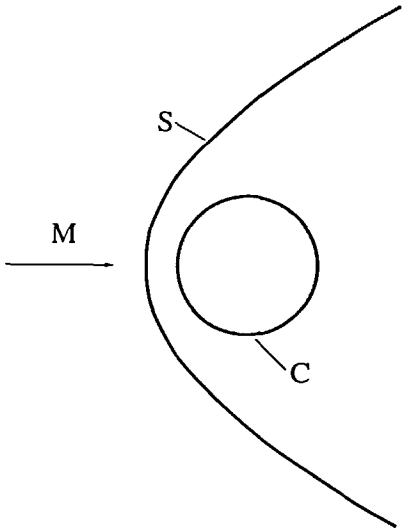

Figure 15 Schematic diagram of blunt-body flow over a circular cylinder; C, circular cylinder; S, bow shock

surface. The predicted angles of the head and tail of the rarefaction wave relative to the horizontal also agree with the values of 20° and 1–2°, respectively, reported by Drewry.

Experimental measurements of the wall density distribution were also made by Drewry using finite-fringe Mach–Zehnder interferometry. (The actual density values were interpreted from the fringe shifts.) However, these data are not included in the comparisons due to uncertainties in the interpretation of the experimental results. Unfortunately, the measured densities were clearly influenced by the presence of a wall boundary layer and viscous effects.

Blunt-body flow in nitrogen

The final test case considered in the evaluation of the proposed TVD schemes is a hypersonic flow around a two-dimensional circular cylinder with its axis of symmetry perpendicular to the free-stream flow direction such that a stationary bow shock forms about the body. This is illustrated in the schematic of *Figure 15*. The free-stream gas is pure nitrogen and the radius of the cylinder is 2.54 cm. The thermodynamic state of the free-stream nitrogen is such that the gas is 7% dissociated (i.e., $c_{N_2} = 0.93$ and $c_N = 0.07$). The free-stream pressure p_∞, density ρ_∞, temperature T_∞, and velocity u_∞ are 2.445 kPa, 5.50×10^{-3} kg/m^3, 1400 K, and 5.5 km/sec, respectively. The frozen-flow Mach number is about 6.9. This blunt-body flow was investigated experimentally by Hornung[68,69]. The infinite-fringe interferogram of the flow field recorded by Hornung using Mach–Zehnder interferometry is given in *Figure 16*. A strong non-equilibrium dissociation process occurs following the bow shock in the stagnation region of the flow and thermal equilibrium conditions are reached in the vicinity of the stagnation point where flow Mach numbers are small. Recent numerical studies have shown that a non-equilibrium analysis is required to accurately predict the density distribution and shock standoff distance for this flow (see, for example, Reference 40) and, therefore, it was felt that the problem would be very appropriate for assessing the fully implicit TVD algorithm.

The preceding blunt-body flow problem was solved by using the fully implicit partially-decoupled TVD scheme on a 100 × 100 grid. The time-stepping, spatial differencing, and compression control parameters used for the calculation are as follows: $\Theta = 1$; $\theta = 0$; and

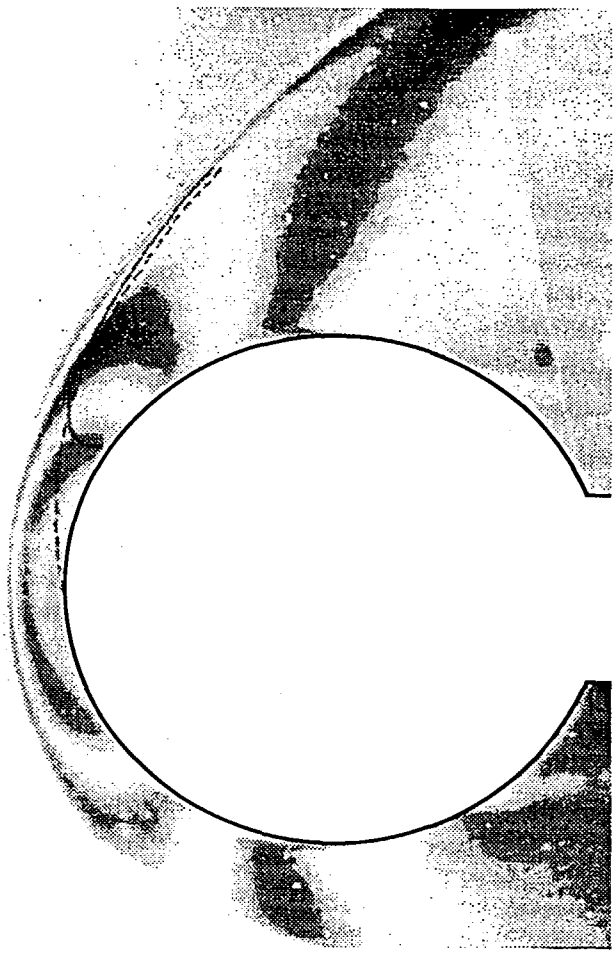

Figure 16 Blunt-body flow; $u_\infty = 5.5$ km/sec, $r = 2.54$ cm, $\rho_\infty = 5.5 \times 10^{-3}$ kg/m^3, $T_\infty = 1{,}400$ K. Interferogram taken from Reference 69, Figure 4

$\beta = 0.75$. A value of 0.30 was used for the entropy parameter $\tilde{\varepsilon}$. A uniform free-stream was assumed for the initial data and the computations were carried out until the measure of the solution residual, $\varepsilon = \sum_i |\Delta\rho_i|/(N_p\rho_i)$, was reduced by three orders of magnitude and velocity of the bow shock approached zero. About 2500 iterations were required to achieve the steady-state solution with the size of the time steps corresponding to a CFL number of about two ($C_{\text{CFL}} = 2$). Shown in *Figure 17* are the isopycnics of the numerical solution. The predicted stagnation temperature and density are approximately 6600 K and 0.066 kg/m^3. Although the fringes of the experimental interferogram do not represent the actual isopycnics, a comparison of *Figures 16* and *17* reveals that the numerical results closely resemble the experimental flow field. The bow-shock standoff distance and shape are both well predicted. Some of the finer details of the density distribution also seem to be reproduced by the fully implicit TVD scheme.

CONCLUSIONS

Semi-implicit and fully implicit extended versions of Roe's and Osher and Chakravarthy's upwind TVD finite-difference schemes have been described for predicting steady and unsteady,

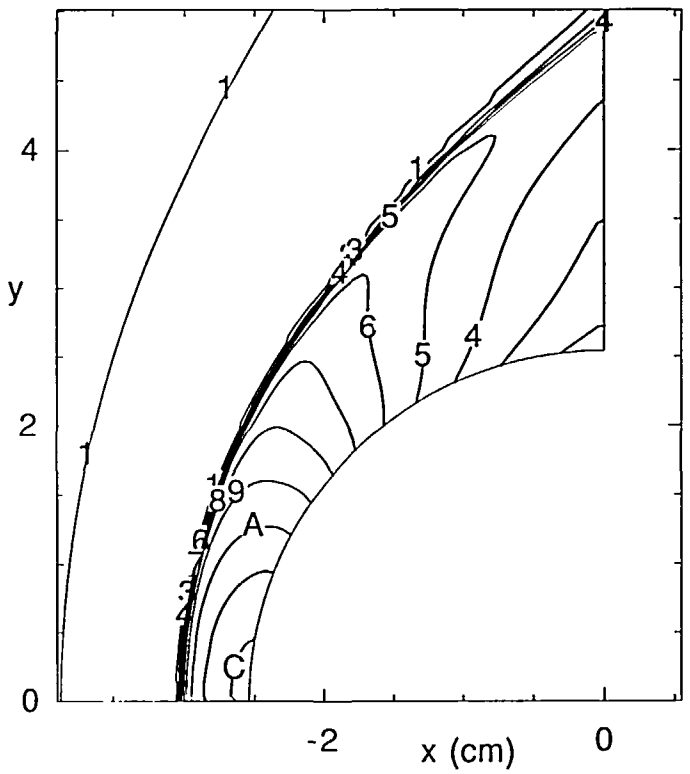

ρ/ρ_0					
	1 1.00	4 4.00	7 7.00	9 9.00	B 11.00
	2 2.00	5 5.00	8 8.00	A 10.00	C 12.00
	3 3.00	6 6.00			

Figure 17 Blunt-body flow; $u_\infty = 5.5$ km/sec, $r = 2.54$ cm, $\rho_\infty = 5.5 \times 10^{-3}$ kg/m^3, $T_\infty = 1{,}400$ K. Predicted constant density contours

two-dimensional, inviscid flows in thermal and chemical non-equilibrium. The proposed schemes solve the governing hyperbolic conservation laws by means of a partially-decoupled FDS approach. This decoupling procedure is shown to offer many of the computational simplifications and savings of uncoupled or chemistry-split procedures while affording the solution quality of fully coupled algorithms (i.e., the solutions are monotonic and positively conservative, and preserve the maximum principle of Larrouturou[46]). Sample numerical computations with comparisons to available experimental data have demonstrated the abilities of the techniques to predict flows with substantial non-equilibrium features and complex shock and non-linear wave structure. Future research will involve enhancing the convergence characteristics of the fully implicit algorithm and extending the schemes for the solution of high-speed viscous flows.

ACKNOWLEDGEMENTS

The work reported herein was completed with the support of the Natural Sciences and Engineering Research Council of Canada (NSERC Research Operating Grant #OGPIN-013). The first author also received financial support in the form of postgraduate scholarships from

the Natural Sciences and Engineering Research Council of Canada and the Ontario Graduate Scholarship Program. All of these funds are gratefully acknowledged. The authors would also like to thank Mr V. Pugliese of UTIAS for helping to reproduce the experimental data.

REFERENCES

1 Boris, J. P. and Book, D. L. Flux-corrected transport. I. SHASTA, a fluid transport algorithm that works, *J. Comput. Phys.*, **11**, 38–69 (1973)
2 van Leer, B. Towards the ultimate conservative difference scheme. V. A second-order sequel to Godunov's method, *J. Comput. Phys.*, **32**, 101–136 (1979)
3 Colella, P. and Woodward, P. R. The piecewise parabolic method (PPM) for gas-dynamical simulations, *J. Comput. Phys.*, **54**, 174–210 (1984)
4 Ben-Artzi, M. and Falcovitz, J. A second-order Godunov-type scheme for compressible fluid mechanics, *J. Comput. Phys.*, **55**, 1–32 (1984)
5 Harten, A. High resolution schemes for hyperbolic conservation laws, *J. Comput. Phys.*, **49**, 357–393 (1983)
6 Harten, A. On a class of high resolution total-variation-stable finite-difference schemes, *SIAM J. Num. Anal.*, **21**, 1–23 (1984)
7 Roe, P. L. Approximate Riemann solvers, parameter vectors, and difference schemes, *J. Comput. Phys.*, **43**, 357–372 (1981)
8 Roe, P. L. and Pike, J. Efficient construction and utilisation of approximate Riemann solutions, *Computing Methods in Applied Science and Engineering VI* (Eds R. Glowinski and J. L. Lions), North-Holland, Amsterdam, pp. 499–518 (1984)
9 Roe, P. L. Generalized formulation of TVD Lax–Wendroff schemes, *ICASE Report No. 84-53* (1984)
10 Davis, S. F. TVD finite difference schemes and artificial viscosity, *ICASE Report No. 84-20* (1984)
11 Yee, H. C. Upwind and symmetric shock-capturing schemes, *NASA TM 89464* (1987)
12 Yee, H. C. Construction of explicit and implicit symmetric TVD schemes and their applications, *J. Comput. Phys.*, **68**, 151–179 (1987)
13 Osher, S. and Chakravarthy, S. R. Very high order accurate TVD schemes, *ICASE Report No. 84-44* (1984)
14 Chakravarthy, S. R. and Osher, S. A new class of high accuracy TVD schemes for hyperbolic conservation laws, *AIAA Paper No. 85-0363* (1985)
15 Chakravarthy, S. R. and Osher, S. Computing with high-resolution upwind schemes for hyperbolic equations, *Large Scale Computations in Fluid Mechanics, Lect. Appl. Math.*, **22**, 57–86 (1985)
16 Harten, A., Enquist, B., Osher, S. and Chakravarthy, S. R. Uniformly high order accurate essentially non-oscillatory schemes, III, *J. Comput. Phys.*, **71**, 231–303 (1987)
17 Colella, P. and Glaz, H. M. Efficient solution algorithms for the Riemann problem for real gases, *J. Comput. Phys.*, **59**, 264–289 (1985)
18 Glaister, P. An approximate linearized Riemann solver for the Euler equations for real gases, *J. Comput. Phys.*, **74**, 382–408 (1988)
19 Glaister, P. An approximate linearized Riemann solver for the three-dimensional Euler equations for real gases using operator splitting, *J. Comput. Phys.*, **77**, 361–383 (1988)
20 Glaister, P. A shock-capturing scheme for body-fitted coordinates, *Int. J. Num. Meth. Fluids*, **8**, 1095–1105 (1988)
21 Vinokur, M. and Liu, Y. Equilibrium gas flow computations. II. An analysis of numerical formulations of conservation laws, *AIAA Paper No. 88-0127* (1988)
22 Grossman, B. and Walters, R. W. Analysis of flux-split algorithms for Euler's equations with real gases, *AIAA J.*, **27**, 524–531 (1989)
23 Montagné, J. L., Yee, H. C. and Vinokur, M. Comparative study of high-resolution shock-capturing schemes for a real gas, *AIAA J.*, **27**, 1332–1346 (1989)
24 Liou, M.-S., van Leer, B. and Shuen, J.-S. Splitting of inviscid fluxes for real gases, *J. Comput. Phys.*, **87**, 1–24 (1990)
25 Suresh, A. and Liou, M.-S. Osher's scheme for real gases, *AIAA J.*, **29**, 920–926 (1991)
26 LeVeque, R. J. and Yee, H. C. A study of numerical methods for hyperbolic conservation laws with stiff source terms, *J. Comput. Phys.*, **86**, 187–210 (1990)
27 Griffiths, D. F., Stuart, A. M. and Yee, H. C. Numerical wave propagation in an advection equation with a nonlinear source term, *SIAM J. Num. Anal.*, **29**, 1244–1260 (1992)
28 Eberhardt, S. and Brown, K. Shock-capturing technique for hypersonic, chemically relaxing flows, *J. Spacecraft*, **24**, 481–488 (1987)
29 Glaz, H. M., Colella, P., Collins, J. P. and Ferguson, R. E. Nonequilibrium effects in oblique shock-wave reflections, *AIAA J.*, **26**, 698–705 (1988)
30 Ben-Artiz, M. The generalized Riemann problem for reactive flows, *J. Comput. Phys.*, **81**, 70–101 (1989)
31 Liu, Y. and Vinokur, M. Nonequilibrium flow computations. I. An analysis of numerical formulations of conservation laws, *J. Comput. Phys.*, **83**, 373–397 (1989)
32 Shuen, J.-S., Liou, M.-S. and van Leer, B. Inviscid flux-splitting algorithms for real gases with non-equilibrium chemistry, *J. Comput. Phys.*, **90**, 371–395 (1990)

33 Yee, H. C. and Shinn, J. L. Semi-implicit and fully implicit shock-capturing methods for nonequilibrium flows, *AIAA J.*, **27**, 299–307 (1989)
34 Bussing, T. R. A. and Murman, E. M. Finite-volume method for the calculation of compressible chemically reacting flows, *AIAA J.*, **26**, 1070–1078 (1988)
35 Gnoffo, P. A. and McCandless, R. S. Three-dimensional AOTV flowfields in chemical nonequilibrium, *AIAA Paper No. 86-0230* (1986)
36 Gnoffo, P. A., McCandless, R. S. and Yee, H. C. Enhancements to program LAURA for efficient computation of three-dimensional hypersolic flow, *AIAA Paper No. 87-0280* (1987)
37 Gnoffo, P. A. Upwind-biased, point-implicit relaxation strategies for viscous, hypersonic flows, *AIAA Paper No. 89-1972-CP* (1989)
38 Molvik, G. A. and Merkle, C. L. A set of strongly coupled upwind algorithms for computing flows in chemical nonequilibrium, *AIAA Paper No. 89-0199* (1989)
39 Slomski, J., Anderson, J. D. and Gorski, J. J. Effectiveness of multigrid in accelerating convergence of multidimensional flows in chemical nonequilibrium, *AIAA Paper No. 90-1575* (1990)
40 Park, C. and Yoon, S. Fully coupled implicit method for thermochemical nonequilibrium air at suborbital flight speeds, *J. Spacecraft*, **28**, 31–39 (1991)
41 Walters, R. W., Cinnella, P., Slack, D. C. and Halt, D. Characteristic-based algorithms for flows in thermochemical nonequilibrium, *AIAA J.*, **30**, 1304–1313 (1992)
42 Anderson, J. D. *Hypersonic and High Temperature Gas Dynamics*, McGraw-Hill, New York (1989)
43 Vincenti, W. G. and Kruger, C. H. *Introduction to Physical Gas Dynamics*, R. E. Krieger Publishing, Huntington, NY (1975)
44 Gnoffo, P. A., Gupta, R. N. and Shinn, J. L. Conservation equations and physical models for hypersonic air flows in thermal and chemical nonequilibrium, *NASA TP 2867* (1989)
45 Vinokur, M. Conservation equations of gasdynamics in curvilinear coordinate systems, *J. Comput. Phys.*, **14**, 105–125 (1974)
46 Larrouturou, B. How to preserve the mass fractions positivity when computing compressible multi-component flows, *J. Comput. Phys.*, **95**, 59–84 (1991)
47 Groth, C. P. T. TVD flux-difference split methods for high-speed thermochemical nonequilibrium flows with strong shocks, *PhD Thesis*, University of Toronto, Institute for Aerospace Studies (1993)
48 Groth, C. P. T., Gottlieb, J. J. and Sullivan, P. Numerical investigation of high-temperature effects in the UTIAS-RPI hypersonic impulse tunnel, *Can. J. Phys.*, **69**, 897–918 (1991)
49 Sweby, P. K. High resolution schemes using flux limiters for hyperbolic conservation laws, *SIAM J. Num. Anal.*, **21**, 995–1011 (1984)
50 Lax, P. D. and Wendroff, B. Systems of conservation laws, *Commun. Pure Appl. Math.*, **13**, 217–237 (1960)
51 Warming, R. F. and Beam, R. M. Upwind second-order difference schemes and application in aerodynamic flows, *AIAA J.*, **14**, 1241–1249 (1976)
52 Murman, E. M. Analysis of embedded shock waves calculated by relaxation methods, *AIAA J.*, **12**, 626–633 (1974)
53 Strang, G. On the construction and comparison of difference schemes, *SIAM J. Num. Anal.*, **5**, 506–517 (1968)
54 Colella, P. Multidimensional upwind methods for hyperbolic conservation laws, *J. Comput. Phys.*, **87**, 171–200 (1990)
55 Thompson, J. F., Warsi, Z. U. A. and Mastin, C. W. *Numerical Grid Generation—Foundations and Applications*, North-Holland, New York (1985)
56 Goodman, J. B. and LeVeque, R. J. On the accuracy of stable schemes for 2D scalar conservation laws, *Math. Comp.*, **45**, 15–21 (1985)
57 Chakravarthy, S. R. Development of upwind schemes for the Euler equations, *NASA CR 4043* (1987)
58 Yee, H. C., Klopfer, G. H. and Montagné, J.-L. High-resolution shock-capturing schemes for inviscid and viscous hypersonic flows, *J. Comput. Phys.*, **88**, 31–61 (1990)
59 Shih, T. I.-P. and Chyu, W. J. Approximate factorization with source terms, *AIAA J.*, **29**, 1759–1760 (1991)
60 Kamowitz, D. Some observations on boundary conditions for numerical conservation laws, *ICASE Report No. 88-67* (1988)
61 Dunn, M. G. and Kang, S. W. Theoretical and Experimental studies of reentry plasmas, *NASA CR 2232* (1973)
62 Millikan, R. C. and White, D. R. Systematics of vibrational relaxation, *J. Chem. Phys.*, **39**, 3209–3213 (1963)
63 Deschambault, R. L. and Glass, I. I. An update on nonstationary oblique-shock-wave reflections: actual isopycnics and numerical experiments, *J. Fluid Mech.*, **131**, 27–57 (1983)
64 Deschambault, R. L. Nonstationary oblique-shock-wave reflections in air, *Univ. Toronto, UTIAS Report No. 270* (1984)
65 Glaz, H. M., Colella, P., Glass, I. I. and Deschambault, R. L. A numerical study of oblique shock-wave reflections with experimental comparisons, *Proc. R. Soc. (A)*, **398**, 117–140 (1985)
66 Drewry, J. E. An experimental investigation of nonequilibrium corner expansion flows of dissociated oxygen, *Univ. Toronto, UTIAS Report No. 124* (1967)
67 Glass, I. I. Theoretical and experimental nozzle and corner expansion flows of dissociated and ionized gases, *Fluid Dyn. Trans.*, **3**, 221–282 (1967)
68 Hornung, H. G. Non-equilibrium dissociating nitrogen flow over spheres and circular cylinders, *J. Fluid Mech.*, **53**, 149–176 (1972)
69 Hornung, H. G. Non-equilibrium ideal-gas dissociation after a curved shock wave, *J. Fluid Mech.*, **74**, 143–159 (1976)